Structural Performance of a Graphite Blanket in Fusion Reactors

W.G. Wolfer and R.D. Watson

June 1978

UWFDM-258

FUSION TECHNOLOGY INSTITUTE

UNIVERSITY OF WISCONSIN

MADISON WISCONSIN

Structural Performance of a Graphite Blanket in Fusion Reactors

W.G. Wolfer and R.D. Watson

Fusion Technology Institute
University of Wisconsin
1500 Engineering Drive
Madison, WI 53706

http://fti.neep.wisc.edu

June 1978

UWFDM-258

"LEGAL NOTICE"

"This work was prepared by the University of Wisconsin as an account of work sponsored by the Electric Power Research Institute, Inc. ("EPRI"). Neither EPRI, members of EPRI, the University of Wisconsin, nor any person acting on behalf of either:

"a. Makes any warranty or representation, express or implied, with respect to the accuracy, completeness, or usefulness of the information contained in this report, or that the use of any information, apparatus, method, or process disclosed in this report may not infringe privately owned rights; or

"b. Assumes any liabilities with respect to the use of, or for damages resulting from the use of, any information, apparatus, method or process disclosed in this report."

STRUCTURAL PERFORMANCE OF

A GRAPHITE BLANKET IN FUSION REACTORS

W.G. WOLFER
R.D. WATSON

Fusion Research Program
Nuclear Engineering Department
University of Wisconsin
Madison WI 53706 U.S.A.

UWFDM-258

I. INTRODUCTION

The integrity of the first wall and the blanket structure behind it is of crucial importance for any fusion reactor. The severe radiation damage to the materials limits the lifetime of these components to less than the plant lifetime. The engineering feasibility of fusion depends to a large extent on the lifetime of the first wall and blanket, and on the ease with which these structures can be replaced. The novel blanket design developed for the SOLASE reactor[14] has the advantage that little pressure is exerted on the blanket structure by the coolant material. Hence, materials other than metals can be selected. Graphite was chosen as a first-wall blanket material because of its great *thermal shock resistance, high melting point, low activity* following neutron activation, and *low cost*. Opposing these advantages are the *low fracture strength* of graphite composites and the *radiation-induced dimensional changes*.

In order to assess the integrity of the first wall and blanket, several sources of stress must be considered. The loading by the *dead weight* of the structure and the coolant is of minor importance in the SOLASE design. Dynamic stresses in the first wall are also produced by the blast wave of the buffer gas in the reactor cavity. The number of radial divider sections in the blanket is selected based on the requirement that the maximum *dynamic stress* associated with the *flexure* of the first wall be below 20.7 MPa (3000 psi). Another source of stress in SOLASE arises from the *absorption of X-rays* emitted from the fusion reaction and from the *absorption of laser light* reflected by the pellet. In both cases, the associated *thermoelastic stress* is restricted to a

depth less than the diameter of the crystallite particles of the graphite composite. Therefore, this surface stress may exceed the composite's fracture stress which is determined by the binder material. It may not, however, exceed the fracture strength of the particles. The latter is an order of magnitude larger than the composite strength. All of the above stress sources will be neglected in the following analysis.

With regard to the long-term integrity of the graphite structure there remain then only two sources: the *static thermoelastic stresses* and those produced by *radiation-induced dimensional changes* due to *temperature* and *flux gradients*. These sources are of *generic* nature and are likely to be encountered in any fusion reactor where graphite is used as a structural material. The following analysis of this problem may be considered also as a case study, and its implications go beyond the particular SOLASE design. In fact, a major objective of this study is to develop a self-consistent methodology for the determination of the lifetime of a graphite structure under irradiation. By self-consistency we refer to the physical interrelations that exist between the radiation-induced porosity changes and the changes in the elastic and strength properties. We also refer to the spacial variation of these properties as they affect the evolution of the stress distribution. The latter in connection with the strength distribution determines then the location and the time of failure.

The immediate objective of the present study is to estimate the lifetime of the blanket structure of the SOLASE reactor, while keeping in mind that the result should not depend on minor design features but rather on more general aspects. Accordingly, we select that part of the blanket structure for the analysis which is subject to the largest temperature and neutron flux gradients. Clearly, this is any one of the radial dividers in a blanket module shown in Fig. 1. To further simplify the analysis the radial divider is modelled as an annular disk.

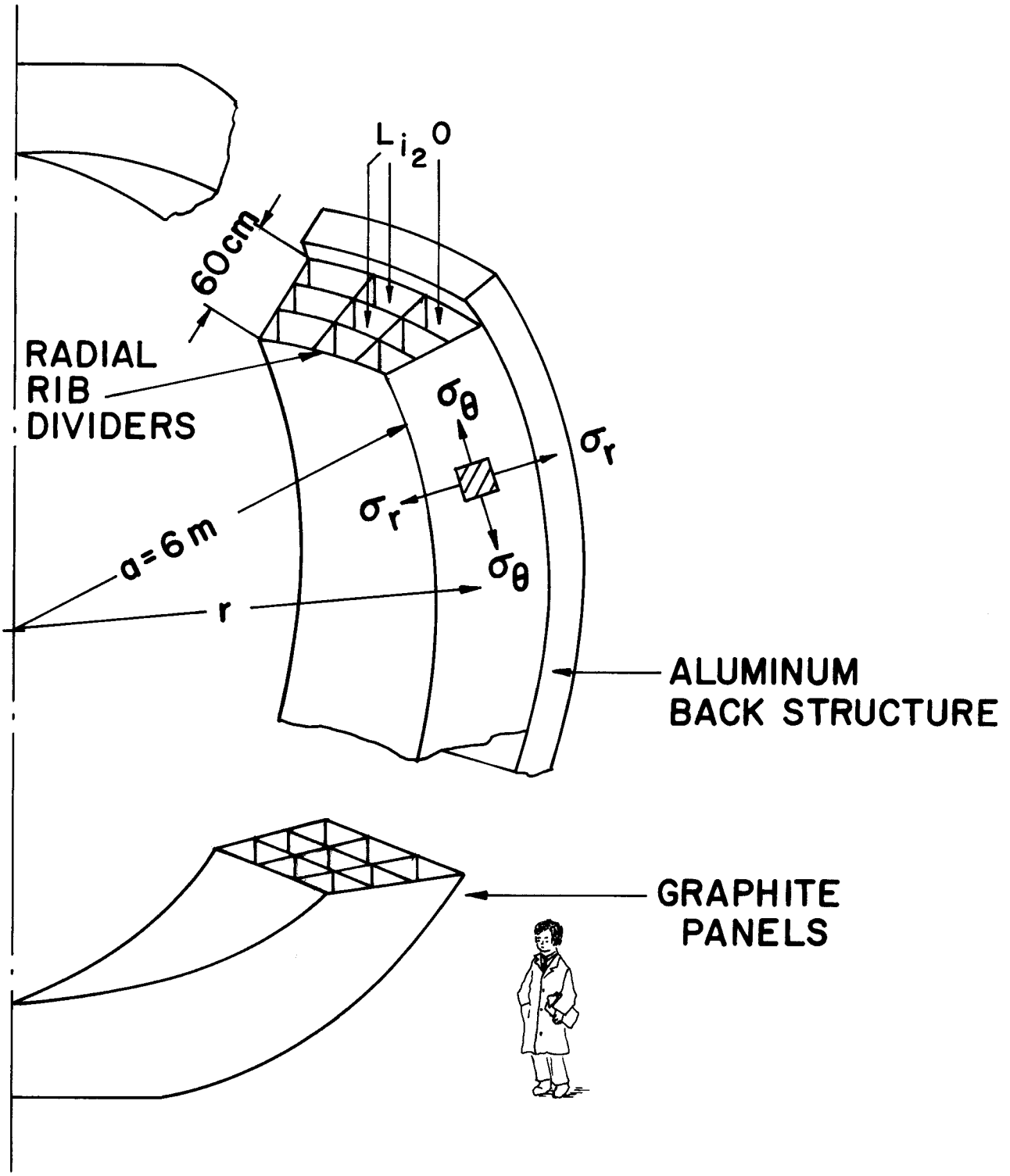

SOLASE BLANKET STRUCTURE-SECTION

FIGURE 1

II. Radiation Effects in Graphite

II.1. Behavior of Point Defects in Graphite

The crystalline structure of graphite, shown in Fig. 2 , is highly anisotropic, and for this reason, the radiation-induced property changes are strongly related to this structure. This is particularly reflected in the migration of interstitials and vacancies. The interstitial, occupying a position between basal planes, has a very low activation energy of 0.45 eV for motion parallel to the basal planes, but a large energy of 2.8 eV for migration in the c-axis direction.[1] Likewise, the vacancy requires an activation energy of about 3 eV to move in the basal plane, but it takes 5.45 eV for motion along the c-axis. The addition of interstitials between basal planes results in a large increase of the lattice parameter "c" relative to the change in the other parameter "a". Contrary, the vacancies do not appreciably alter the c- spacing but give rise to a decrease in the a - spacing according to[2]

$\Delta a/a = -0.14\ n_v$, where n_v is the number density of vacancies.

Since in the production of interstitial-vacancy pairs by energetic recoil atoms the point defect pair is spacially separated, a correlated recovery is very unlikely unless the point defects are situated on the same basal plane. Consequently, the predominant reaction at high temperatures will be the formation of separate interstitial and vacancy clusters. As a result, the growing interstitial loops produce additional basal planes, whereas the old basal planes contract. Hence, each single-crystal region

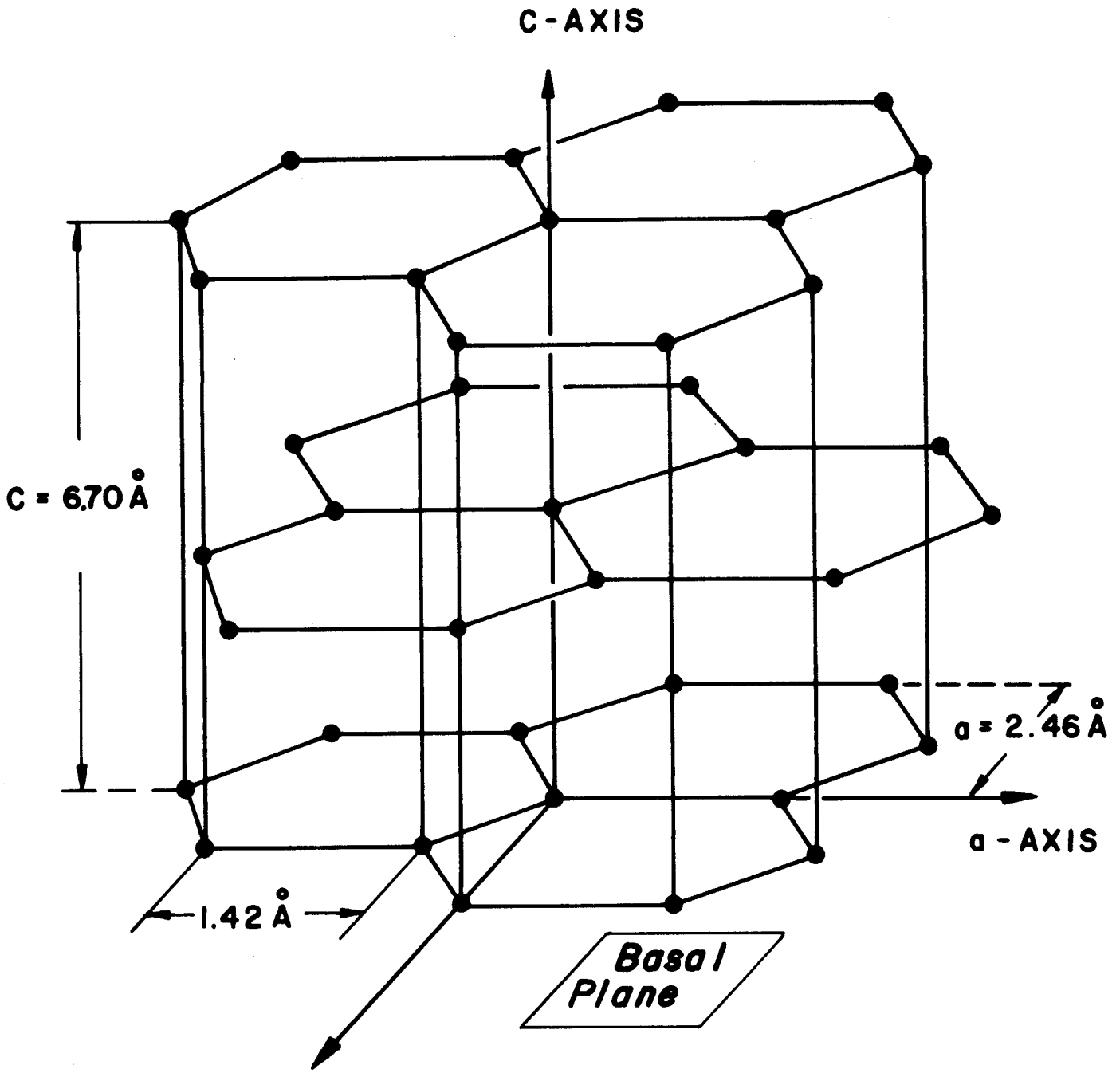

Fig. 2 -- Crystalline Structure of Graphite

in a graphite solid under irradiation will expand in the c-direction and contracts in the a-direction.

II.2 Dimensional Changes of Polycrystalline Graphites

Polycrystalline graphites exhibit large dimensional changes after irradiation. These dimensional changes depend strongly on the raw material and the fabrication process used. As illustrated in Figs. 3,4,5,& 6 these changes are characterized by an initial densification followed by an expansion at higher radiation doses.

This phenomenon can be explained by the dimensional changes of the graphite crystallites that make up the graphite particles and by the closure and expansion of pores and microcracks. Following the notation of Engle[3], there are three different types of pores (see Fig. 7). The crystallites themselves contain micropores which contribute the volume ΔV_{p_1} to the total porosity. Many crystallites are contained in a single graphite particle, and transgranular microcracks between the crystallites occupy a volume ΔV_{p_2}. In turn, the particles are held together by a graphite binder, produced from coal-tar pitch, and they may enclose intergranular microcracks which take up the volume ΔV_{p_3}.

During irradiation the individual crystallites expand in the c-direction, i.e. perpendicular to the basal planes, but contract parallel to the basal planes (or in the a-direction). As a result, the different pore volumina change with time. Initially, the dimensional changes are produced by a partial closure of all three pore types. However, as the crystallites continue to expand in the c-directions, new and old microcracks open up, causing ΔV_{p_2} and ΔV_{p_3} to increase.

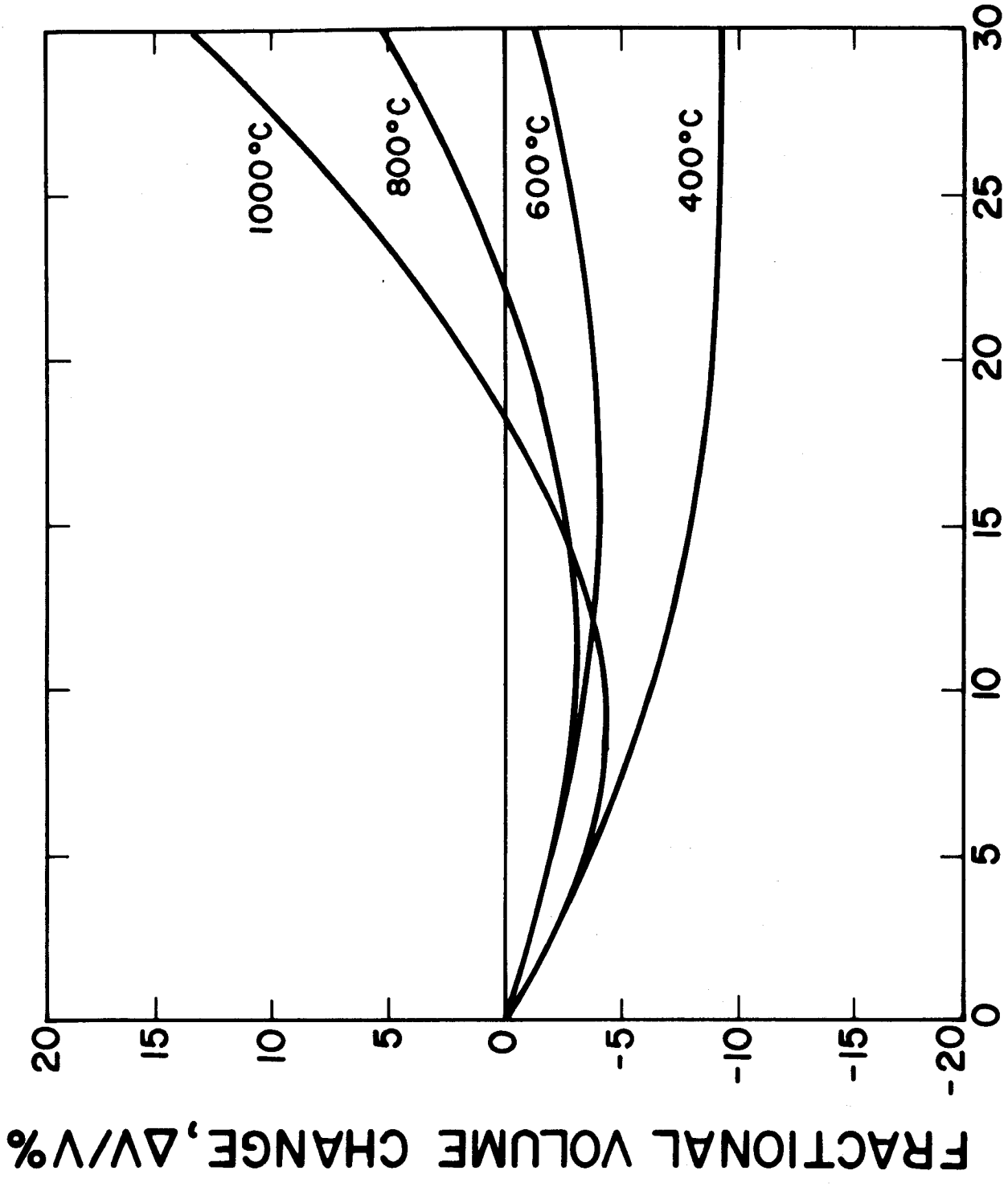

Fig. 3 -- Volume Change of Graphite with 20% Initial Porosity Irradiated at Temperatures between 400°C and 1000°C

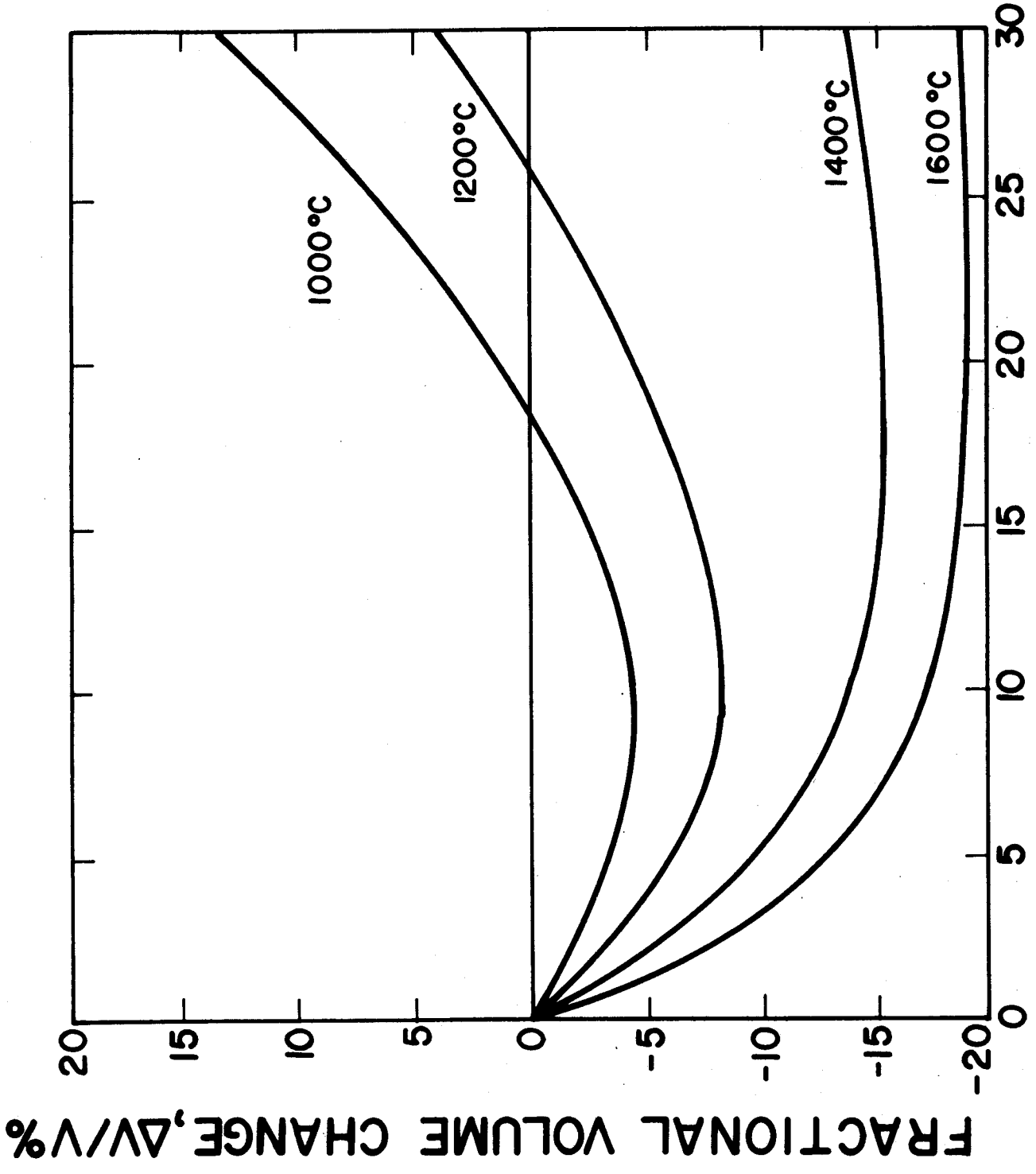

Fig. 4 -- Volume Change of Graphite with 20% Initial Porosity Irradiated at Temperatures between 1000°C and 1600°C

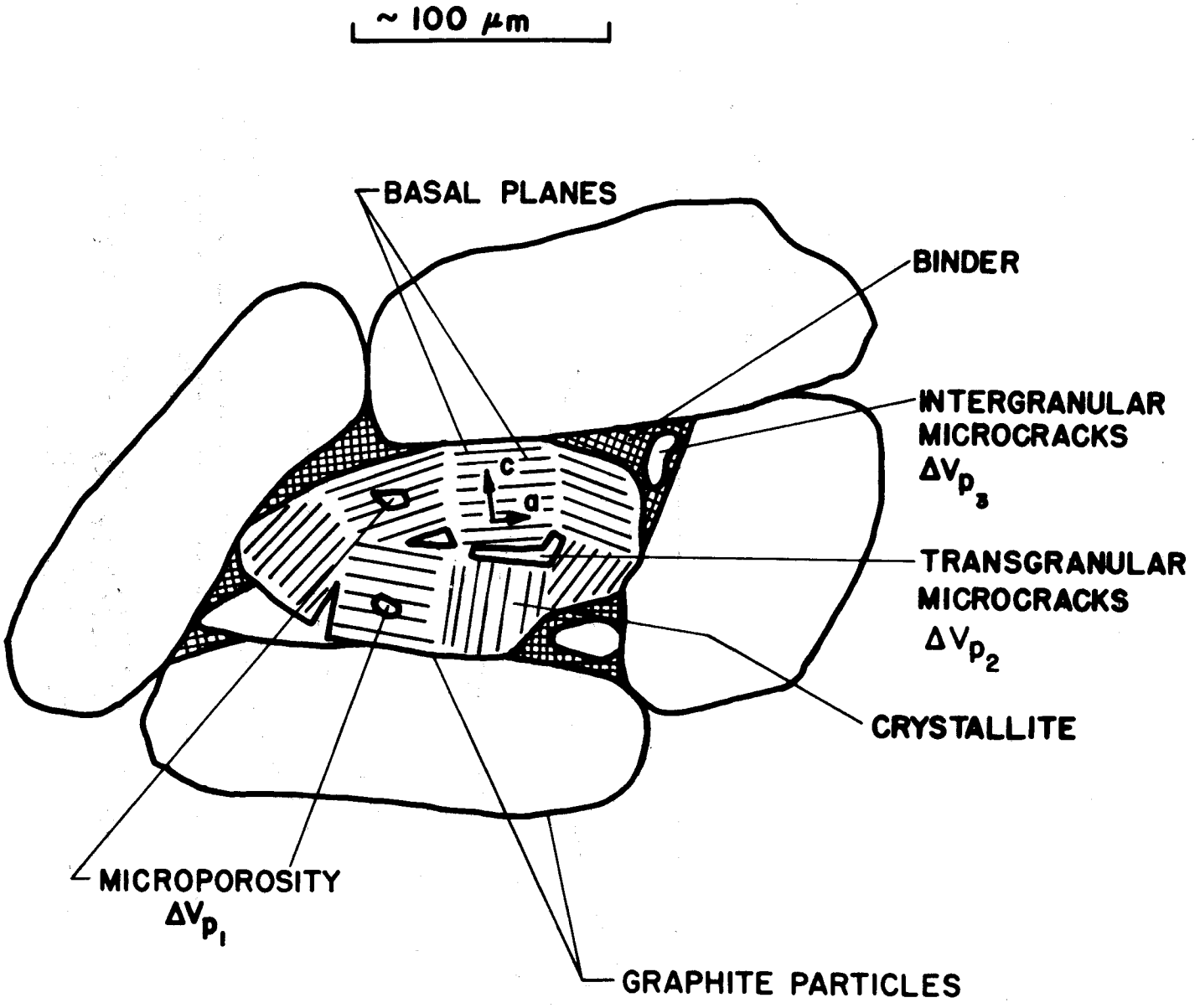

Fig. 7 -- Microstructure of Polycrystalline Graphite

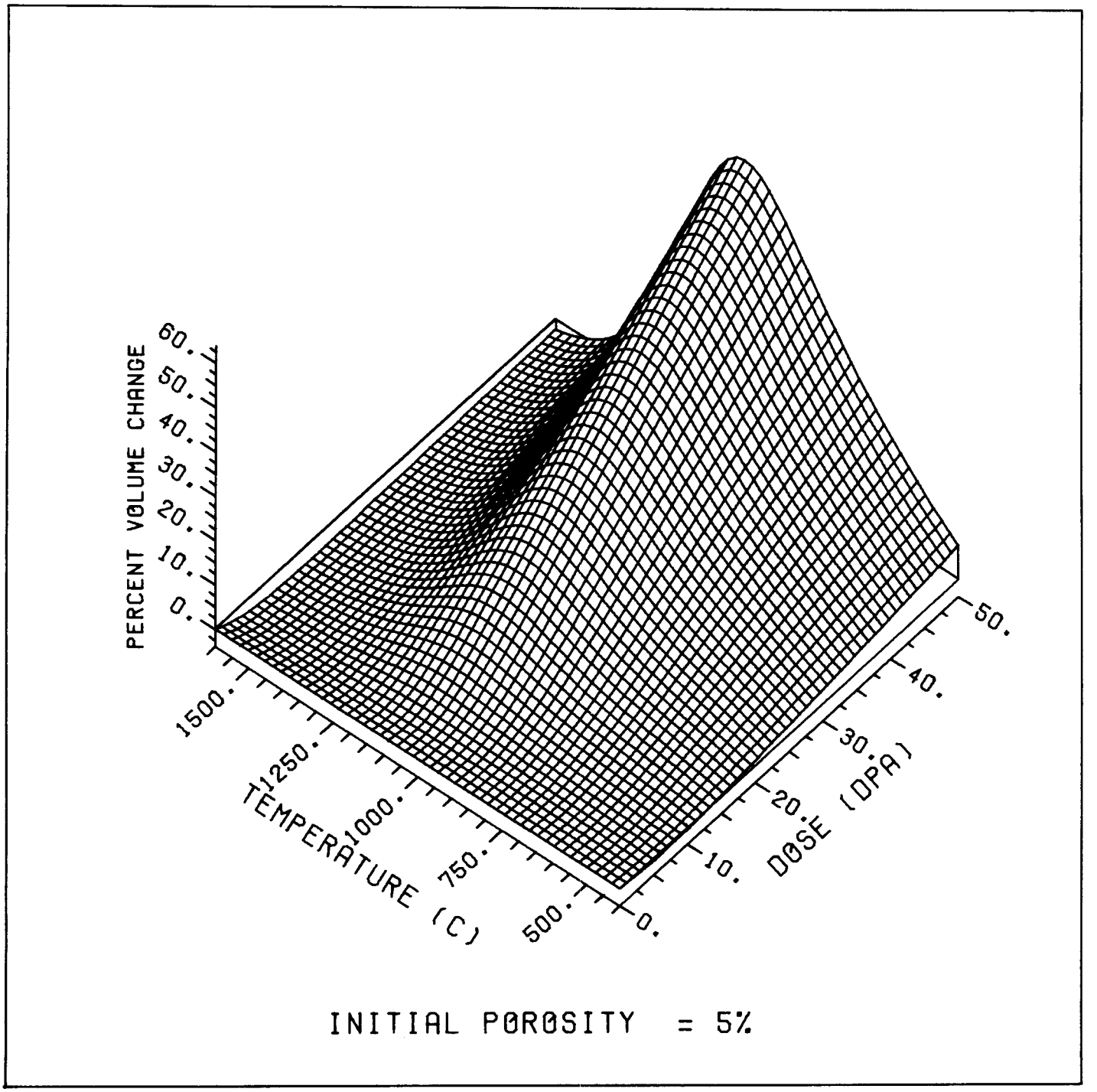
PERCENT VOLUME CHANGE
60.
50.
40.
30.
20.
10.
0.
1500.
1250.
1000.
750.
500.
TEMPERATURE (C)
0.
10.
20.
30.
40.
50.
DOSE (DPA)
INITIAL POROSITY = 5%

FIGURE 5

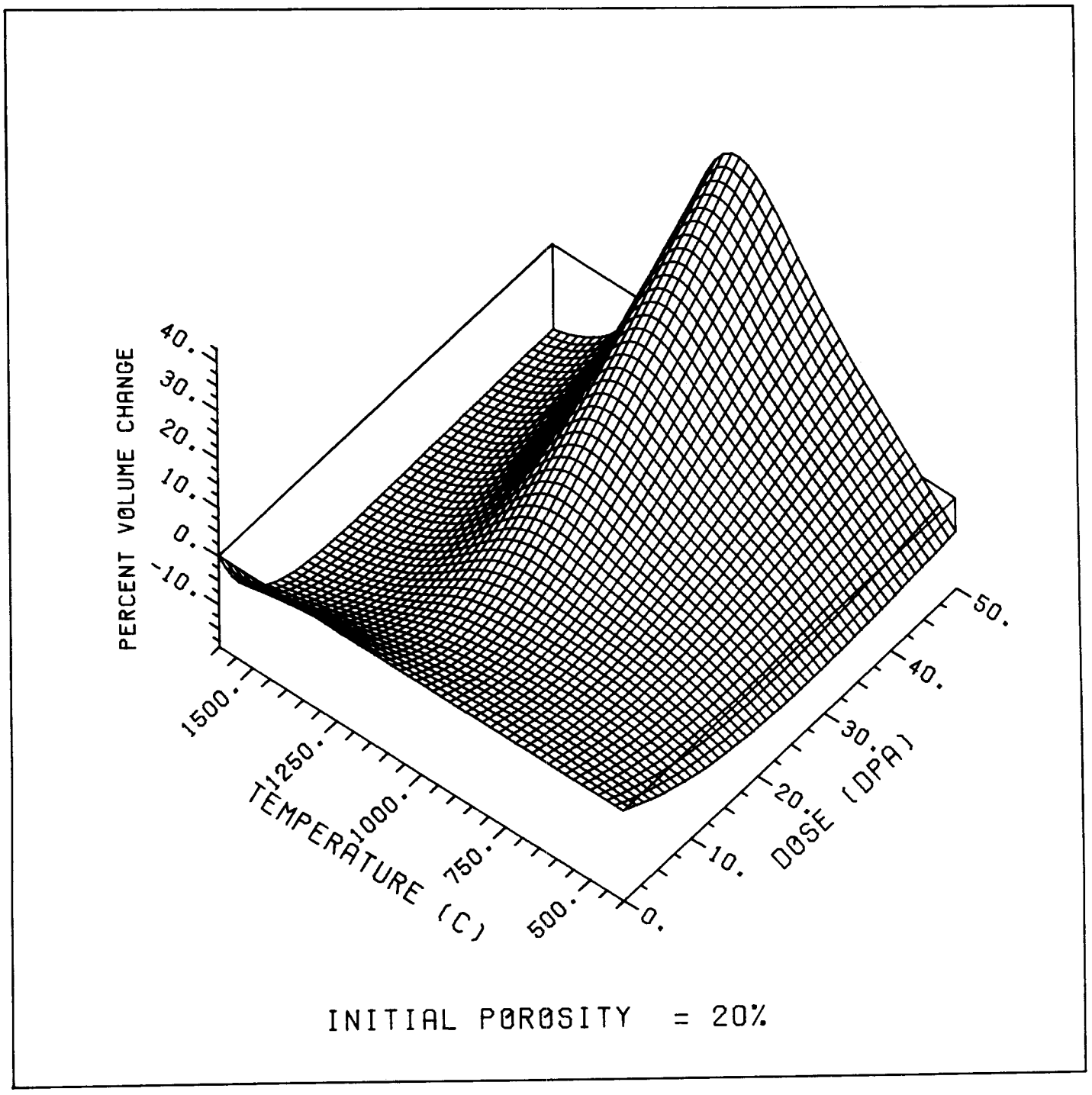
PERCENT VOLUME CHANGE
40.
30.
20.
10.
0.
-10.
1500.
1250.
1000.
750.
500.
TEMPERATURE (C)
0.
10.
20.
30.
40.
50.
DOSE (DPA)
INITIAL POROSITY = 20%

FIGURE 6

The contribution of the three different types of pores has been measured as a function of irradiation dose by Engle.[3] This was accomplished in the following way. First, the total volume change

$$\Delta V = \Delta V_{p_1} + \Delta V_{p_2} + \Delta V_{p_3} \qquad (1)$$

was determined by length change measurements. After that the specimens were immersed in a liquid thereby filling the porosity ΔV_{p_3}. The measurement gave then $\Delta V_{p_1} + \Delta V_{p_2}$. Finally, the graphite was crushed into its particles, and the powder was again immersed in a liquid. Because the liquid penetrated the pore volume ΔV_{p_2}, the volume ΔV_{p_1} could then be found.

In summary, Engle was able to describe dose dependence of the three porosity contributions. He found that ΔV_{p_1} increases slightly initially and changes little thereafter. However, ΔV_{p_2} decreases initially, contributing mostly to the initial densification phase, and then increases moderately at higher doses. The pore volume ΔV_{p_3} changes little during the densification phase but then increases dramatically. Therefore, ΔV_{p_3} is the major contributor to the final expansion rate of graphite under irradiation.

In the manufacture of graphite components, the selected coke particles are combined with the binder material, and the components are formed at high temperatures either by extrusion or by molding. In the extrusion process, the particles and crystallites arrange themselves in such a fashion that there results a preferential orientation of the c-axis perpendicular to the extrusion direction. If the component is molded, the c-axis aligns itself parallel to the pressure direction.

The resulting composite exhibits anisotropic behavior. The direction which is predominantly influenced by the c-axis properties suffers an initial contraction followed by expansion at high exposures. On the other hand, the directions predominantly aligned with the a-axis of the crystallites continue to contract up to much higher exposures before the expansion begins. By proper selection of raw material and processing steps, it is possible to produce graphites with macroscopically isotropic properties.

The change of porosity in graphite as a function of irradiation is accompanied by corresponding changes in the strength, elastic properties, thermal expansivities, thermal conductivity and most other physical properties. Hence, it was important to develop a quantitative model for the dimensional changes of graphites which are used for structural purposes. As discussed above, one can rationalize the dimensional changes by a two-step process. Initially, the densification is mainly due to a partial closure of the fabricated porosity which accomodates the dimensional changes of the crystallites. After exhaustion of this process, further accomodation can only be accomplished by creation of new,and enlargement of, existing micro-cracks between the particles and crystallites. It is then reasonable to assume that the initial densification rate is proportional to the initial porosity, P_o, but the final expansion rate should not depend on P_o. However, the onset of expansion is delayed with increasing initial porosity P_o.

A phenomenological equation, reflecting this behavior, is given by

$$P - P_o = \frac{\Delta V}{V_o} = \frac{A F^{n+1}}{BP + F^n} - P_o[1 - \exp(- CF)] \qquad (2)$$

where F is the radiation dose, and A, B, C and n are materials parameters which must be determined by fitting Eq. (2) to the experimental data. The particular dose dependence chosen for the first term in Eq. (2) is based on the assumption that the volumetric expansion will eventually become linear with dose. At present, there are no data at high doses available that either contradict or confirm this conjecture. However, it appears reasonable to assume that the expansion of the crystallites along their c-axis must eventually be linear with dose.

It has already been mentioned that the different graphites vary as far as their dimensional changes are concerned. Therefore, no attempt was made to fit Eq. (2) to any particular graphite. Instead, we strived for a description that is generic rather than specific. Accordingly, by inspection of available data and various equations of the form of Eq. (2) it was determined that the following equation is most compatible with the entire body of data utilized. This equation is

$$P - P_o = \frac{\Delta V}{V_o} = \frac{A F^3}{P_o/C + F^2} - P_o[1 - \exp(- CF)] \qquad (3)$$

It contains now only two parameters, A and C, which must be determined from experimental data. The most convenient way to accomplish this is to compare the initial shrinkage rate and the final growth rate with the data. Since

$$dP/dF = AF^2 \frac{3P_o/C + F^2}{(P_o/C + F^2)^2} - P_o C \exp(- CF) \qquad (4)$$

the initial shrinkage rate is given by

$$\dot{P}_i = (dP/dF)|_{F=0} = -P_o C \tag{5}$$

and the final growth rate is

$$\dot{P}_f = (dP/dF)|_{F\to\infty} = A. \tag{6}$$

The data that were used to determine A and C were length changes of anisotropic graphites. Therefore, the volume changes $\Delta V/V_o$ were computed from the length changes $(\Delta L/L)_{\parallel}$ parallel and the length changes $(\Delta L/L)_{\perp}$ perpendicular to the extrusion direction according to the formula

$$P - P_o = \frac{\Delta V}{V_o} = \left(\frac{\Delta L}{L}\right)_{\parallel} + 2\left(\frac{\Delta L}{L}\right)_{\perp} . \tag{7}$$

Conversion from fluence units to displacement units (dpa) were made according to correlations of Morgan.[4] The final growth rates for the length changes were estimated from the curves reported in the literature, and the volumetric growth rates were then computed with Eq. (7). These values are listed in Table 1 and plotted in Fig. 8. The same procedure was followed for obtaining the initial shrinkage rates. The corresponding values are given in Table 2 and plotted in Fig. 9.

According to Fig. 8, it appears that one can divide the different graphites into two groups. The group comprising the majority of the data in Fig. 8 has a modest final growth rate with a maximum of about $1.5(\frac{\Delta V}{V_o}\%)$/dpa at 1000°C. Both data groups were fitted to simple analytical expressions. For the low-growth graphites

$$A = \dot{P}_f = \{(\frac{800}{T})^2 + (\frac{T}{1250})^{12}\}^{-1} \quad [\frac{\Delta V}{V_o}\%/\text{dpa}] \tag{8}$$

where T is the temperature in °C, and for the high growth graphites

Table 1

Final Volumetric Growth Rates of Graphites

Graphite	Ref.	Temp. (°C)	$\dot{P}_f$ [%/dpa]	Symbol
Gilso	5	1125	1.03	●
		1150	1.44	
		1300-1500	0.20	
Petro-coke	5	1125-1150	1.32	○
		1175-1200	1.14	
		1300-1350	0.26	
		1400-1425	0.16	
Nuclear Grade	6	400-475	0.14	▬
		650-750	1.42	
		950-1050	6.78	
		1200-1300	0.68	
Improved Isotropic	6	715	0.68	x
		950-1060	1.36	
Extruded Gilso	7	1400	1.25	▲
Pitch-coke	7	1400	3.90	✦

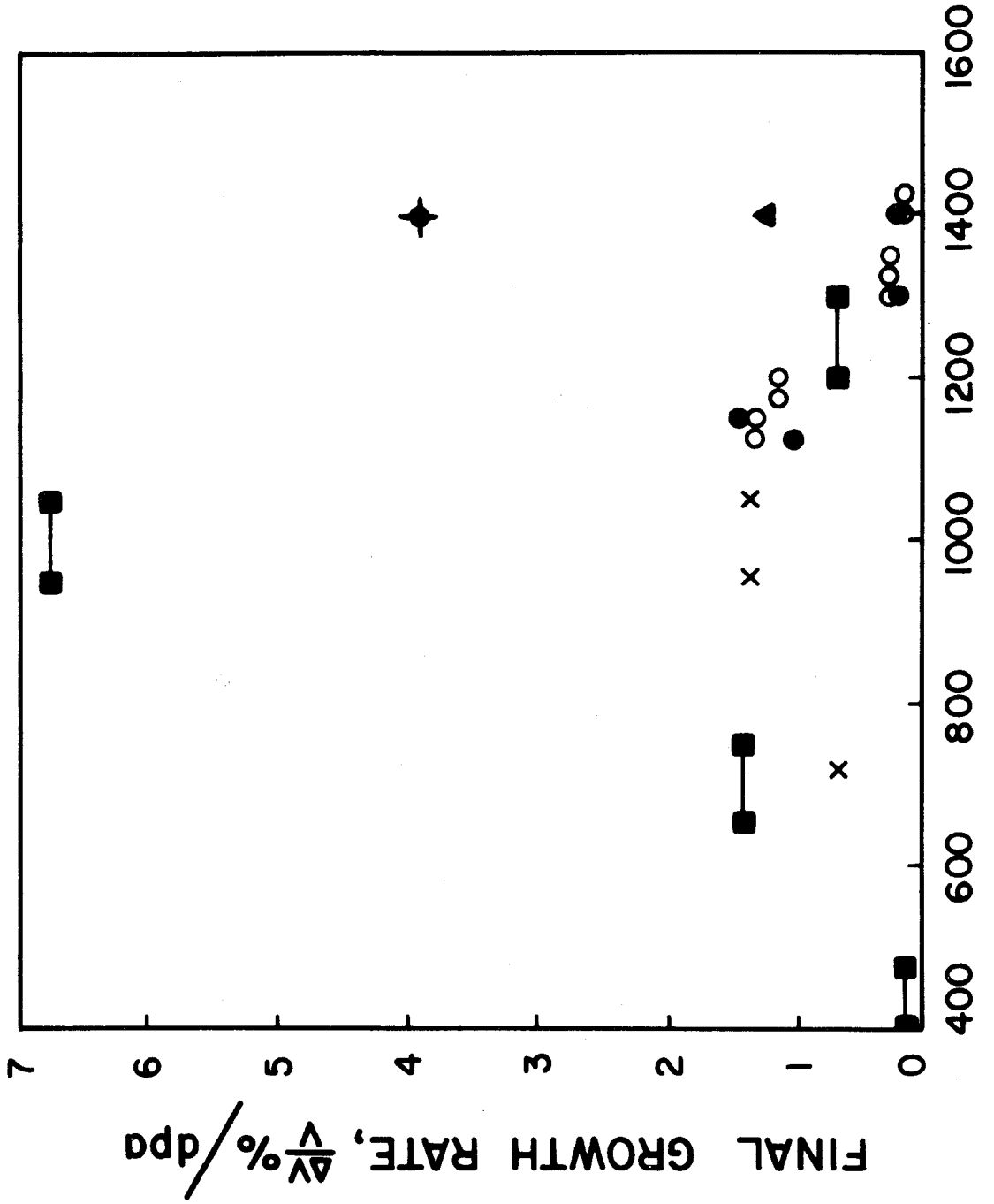

Fig. 8 -- Final Volumetric Growth Rate of Graphites as a Function of Irradiation Temperature. (For Meaning of Symbols see Table XV-A-1)

Table 2

Initial Volumetric Shrinkage Rates of Graphites

Graphite	Ref.	Temp. Range (°C)	$-\dot{P}_i/P_o$ [dpa^{-1}]	Symbol
Gilso	5	1125-1400	$0.096^{+0.031}_{-0.020}$	●
Petro-coke	5	1125-1425	$0.105^{+0.035}_{-0.024}$	o
Nuclear Grade	6	400-475	$0.036^{+0.012}_{-0.007}$	■
		650-750	$0.024^{+6.008}_{-0.005}$	
		950-1050	$0.045^{+0.025}_{-0.009}$	
		1200-1300	$0.068^{+0.032}_{-0.014}$	
Improved Isotropic	6	715	$0.0024^{+0.0008}_{-0.0004}$	X
		950-1300	$0.0068^{+0.0022}_{-0.0014}$	
Extruded Gilso	7	500	0.028	▲
		600	0.026	
		700	0.024	
		800	0.031	
		900	0.059	
		1000	0.074	
		1100	0.039	
		1200	0.067	
		1300	0.120	
		1400	0.170	
		1500	0.215	

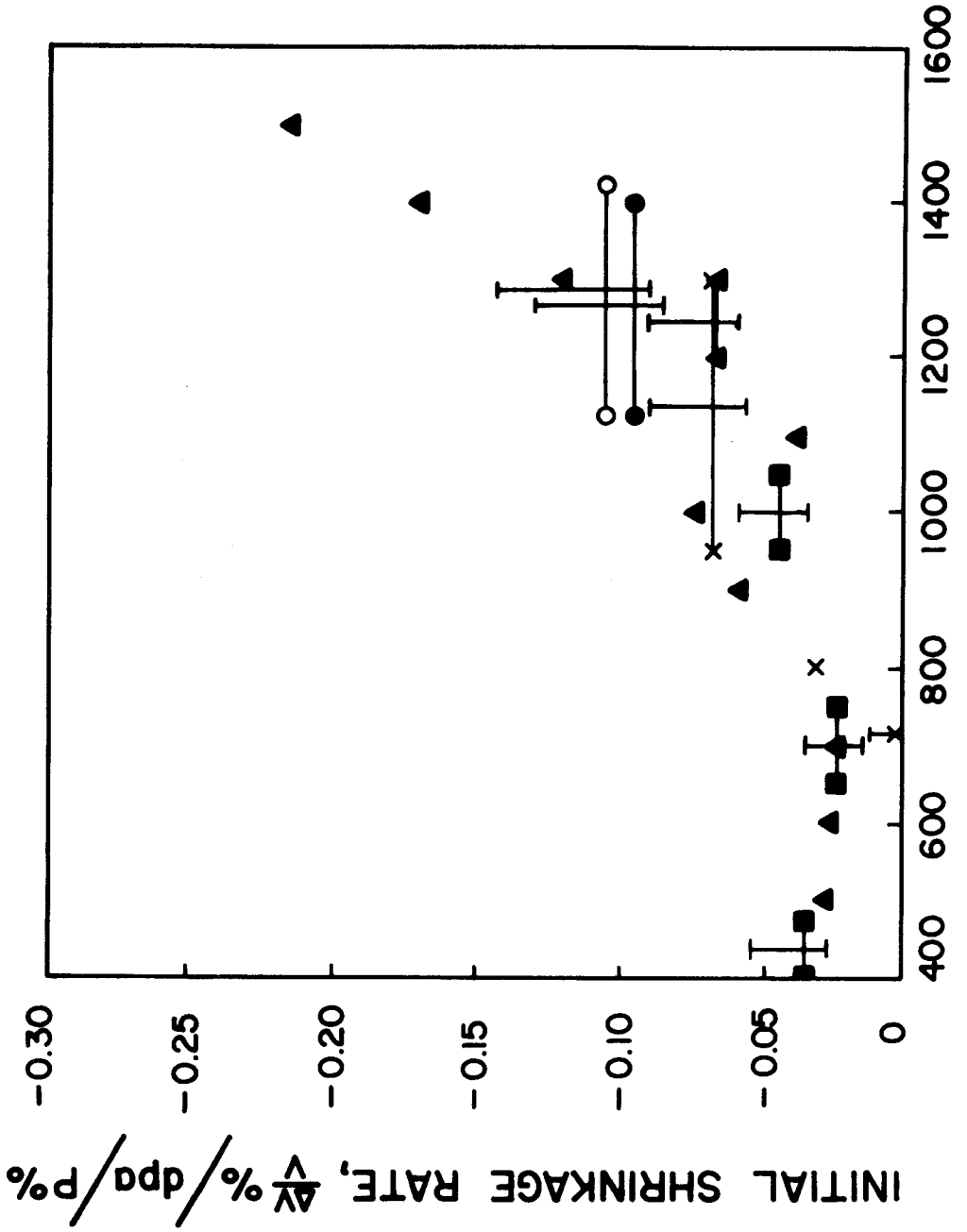

Fig. 9 -- Initial Volumetric Shrinkage Rate of Graphites as a Function of Irradiation Temperature. (For Meaning of Symbols see Table XV-A-2)

$$A = \dot{P}_f = 9.4 \left\{\left(\frac{900}{T}\right) + \left(\frac{T}{1050}\right)^4\right\}^{-1} \left[\frac{\Delta V}{V_o} \% \text{ /dpa}\right] \quad (9)$$

Plots of Eqs. (8) and (9) are shown in Figs. 10 and 11, respectively.

In contrast to the distinction in the final growth rate, the graphites considered for this study do not differ in their initial shrinkage rates, as can be clearly seen from Fig. 9. Therefore, all the data can be fitted to one expression. The nominal or average fit is simply given by

$$C = -\dot{P}_i/P_o = 0.01 \left(\frac{T-700}{210}\right)^2 + 0.02 \quad (9a)$$

A lower bound can be obtained from

$$C = \dot{P}_i/P_o = 0.01 \left(\frac{T-700}{230}\right)^2 \quad (9b)$$

And an upper bound from

$$C = -P_i/P_o = 0.01 \left(\frac{T-700}{170}\right)^2 + 0.04 \quad (9c)$$

All three expressions are plotted in Fig. 12. The volumetric changes for the model graphite, as given by Eq. (3), are shown in Figs. 3,4,5,and 6 for the low-growth graphite (A given by Eq. (8) and C given by Eq. (9)).

II.3 Irradiation Creep of Graphite

Concurrent with the dimensional changes, graphite also exhibits radiation-enhanced creep when subject to either external loads or self-generated stresses due to non-uniform dimensional changes. A recent review and discussion of the data has been given by Blackstone.[8] The creep rate $d\varepsilon/dF$ of graphite under irradiation is a linear function of the stress σ, i.e.

$$\frac{d\varepsilon}{dF} = K\sigma \quad (10)$$

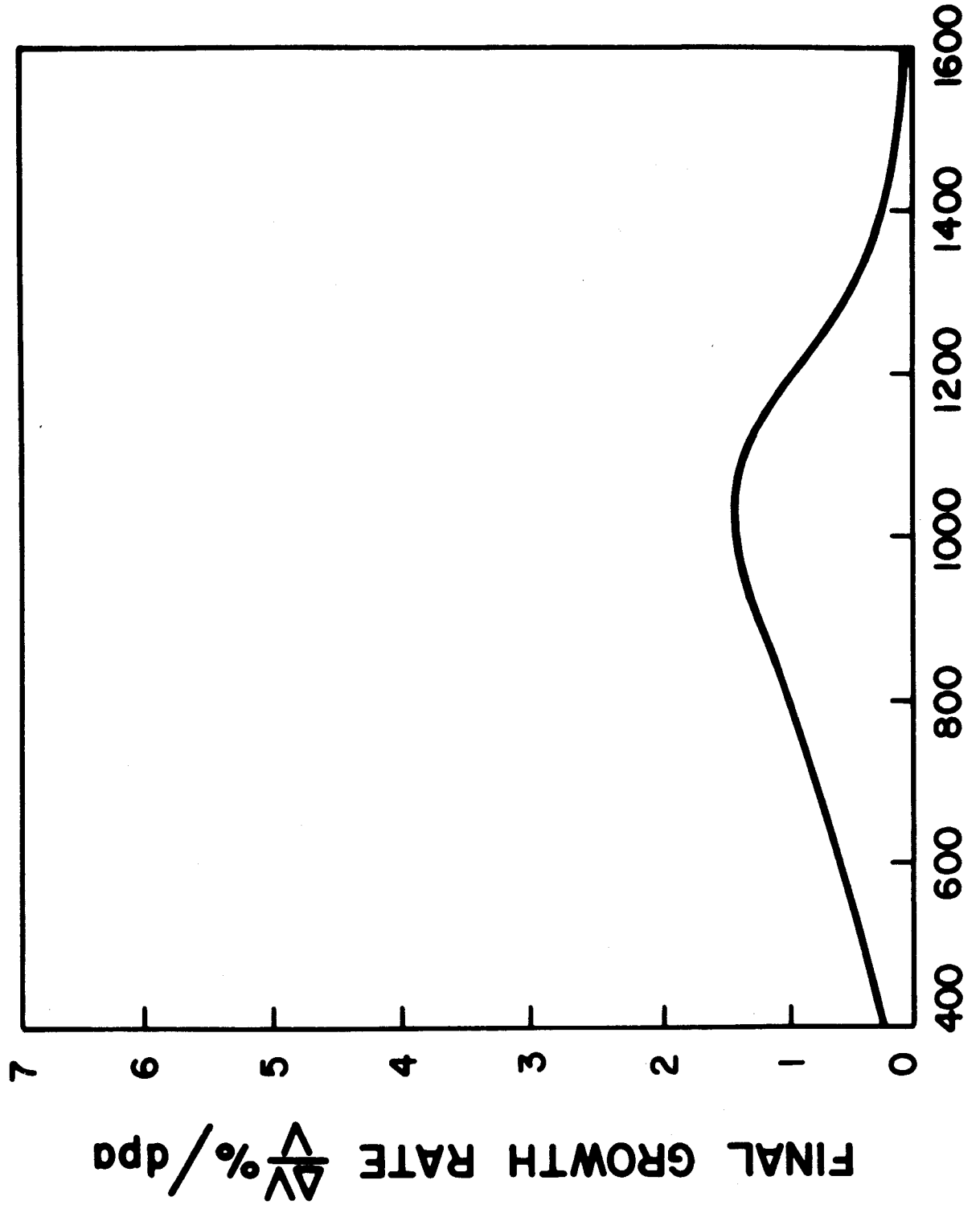

Fig. 10 -- Final Volumetric Growth Rate according to Eq. (8)

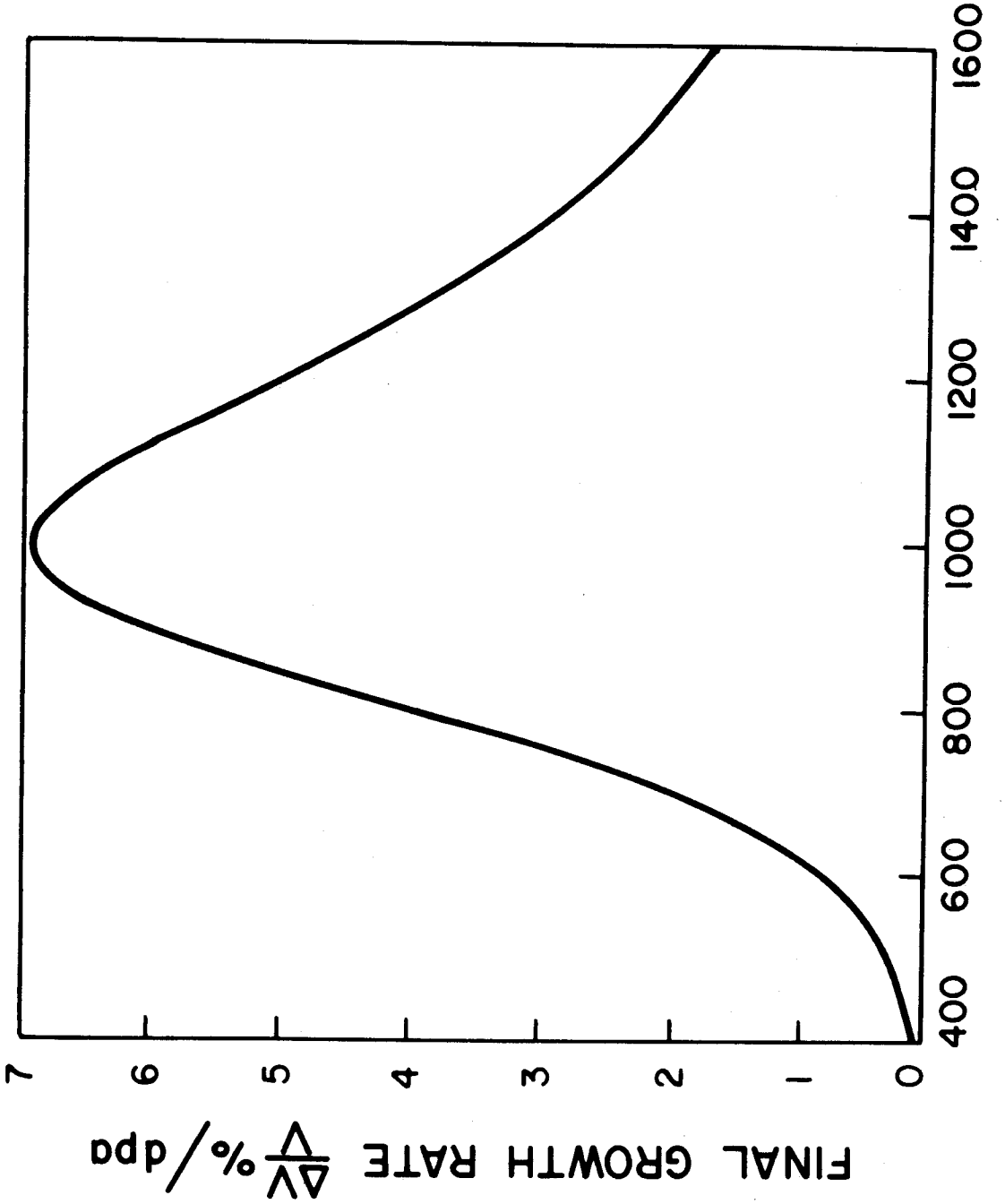

Fig. 11 -- Final Volumetric Growth Rate according to Eq. (9)

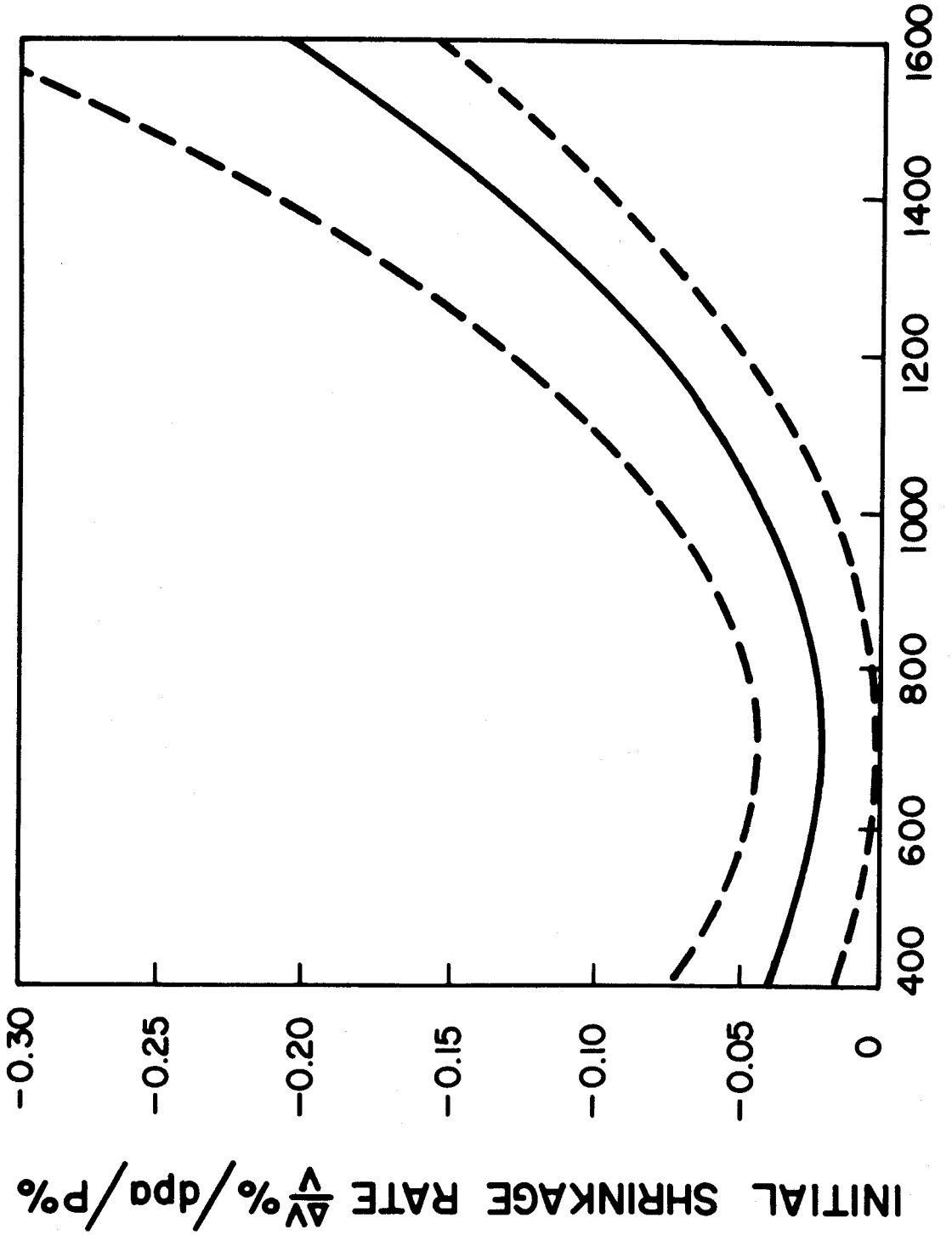

Fig. 12 — Initial Volumetric Shrinkage Rates of Graphites according to Eqs. (9), (9a), and (9b).

where F is the dose. Veringa and Blackstone[9] have shown that a satisfactory correlation of most irradiation creep data can be obtained when the product of the creep coefficient K and the initial Young's modulus E_o is plotted as a function of the irradiation temperature T, as shown in Fig. 13. The data can then be correlated with the expression

$$KE_o = \frac{f(T)}{\dot{F}} + g(T) \tag{11}$$

where f(T) and g(T) are linear functions of the temperature and are given by

$$f(T) = (1.775 + 0.0185*T) \times 10^{-8} \text{ sec}^{-1} \tag{12}$$

and

$$g(T) = (-0.544 + 0.00403*T) \text{ dpa}^{-1} \tag{13}$$

Even though the creep correlation of Eq. (11) is based on the initial elastic modulus, E_o, the data can be equally well correlated with the final elastic modulus after the irradiation. In fact, since the elastic modulus changes as a function of the porosity, we presume that Eq. (11) should actually read

$$KE = \frac{f(T)}{\dot{F}} + g(T) \tag{14}$$

where E is the instantaneous elastic modulus. It should be noted that the transient or primary part of the irradiation creep has been neglected

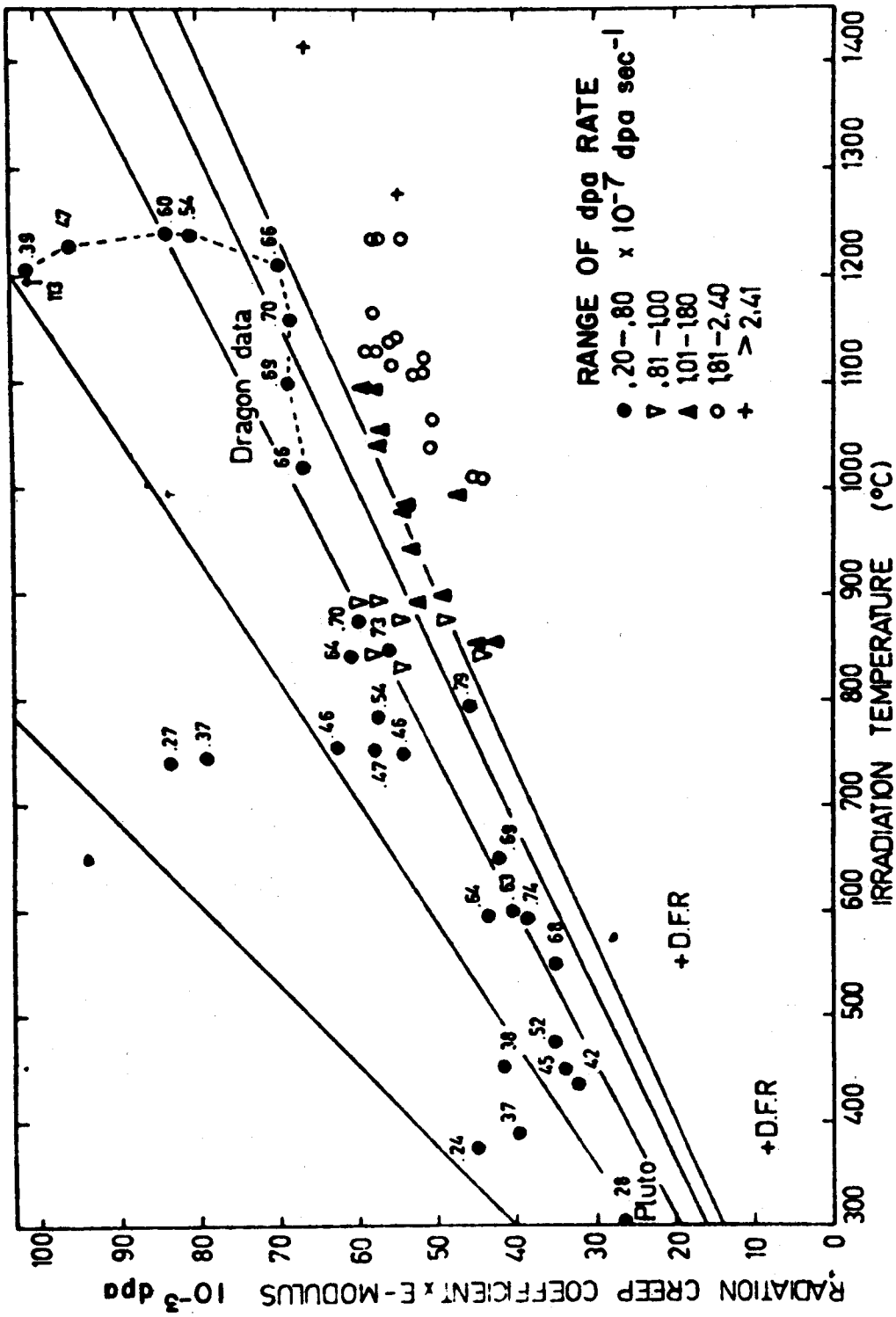

Fig. 13 -- The Product of Irradiation Creep Constant and Young's Modulus for Different Dose Rates and Different Irradiation Temperatures.

in Eq. (10) since it is of little consequence in the forthcoming analysis.

II.4 Changes of Elastic Properties and Strength

Fast neutron irradiation produces changes in both elastic modulus and ultimate strength. Initially, both increase rapidly but then level off after a dose of about 1 dpa. Further changes take place more slowly, and they are accompanied by the corresponding dimensional changes. The initial rapid rise of the elastic modulus is commonly attributed to dislocation pinning by defect clusters within the crystallites, whereas the latter changes appear to be related to the changes in the porosity volumes of ΔV_{p_2} and ΔV_{p_3}. Fig. 14 shows the change of Young's modulus as a function of the fast neutron dose.[10]

The change in the tensile fracture stress is depicted[10] in Fig. 15 together with empirical fit of the form

$$\frac{\sigma}{\sigma_o} = \left(\frac{E}{E_o}\right)^n \tag{14}$$

It can be seen that a satisfactory correlation exists between σ and E for n = 1/2. This square-root relationship follows also from the Griffith fracture formula

$$\sigma = \sqrt{2E\gamma/\pi C} \tag{15}$$

where γ is the effective surface energy for fracture, and 2C is the length of the largest crack. This length can be expected to be of the order of the grain or graphite particle diameter. Hence, if we assume that 2C as

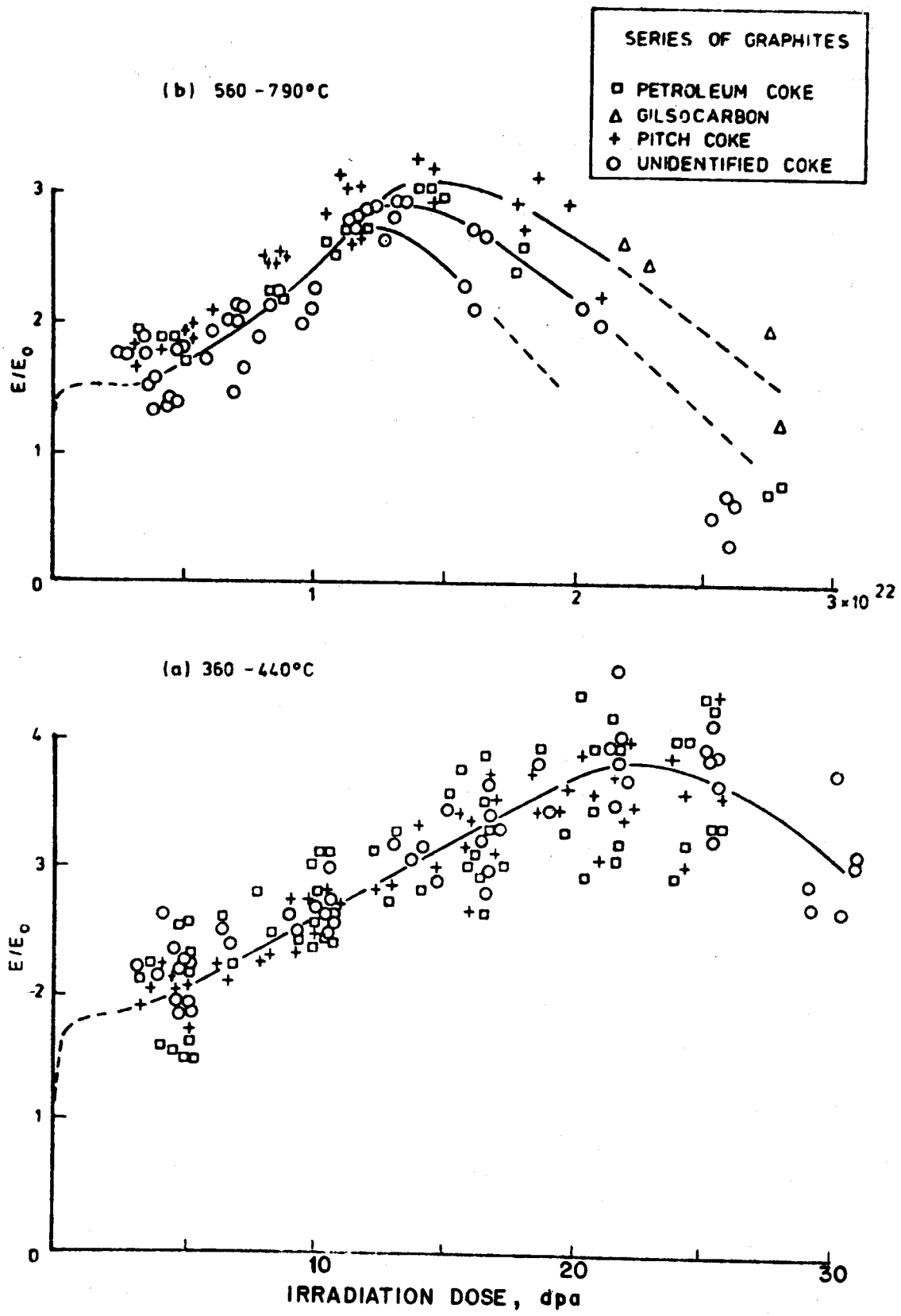

Fig. 14 -- Young's Modulus Changes with Fast-Neutron Dose for Different Near-Isotropic Graphites Irradiated in DFR (a) at Irradiation Temperature from 360 to 440°C and (b) from 560 to 790°C

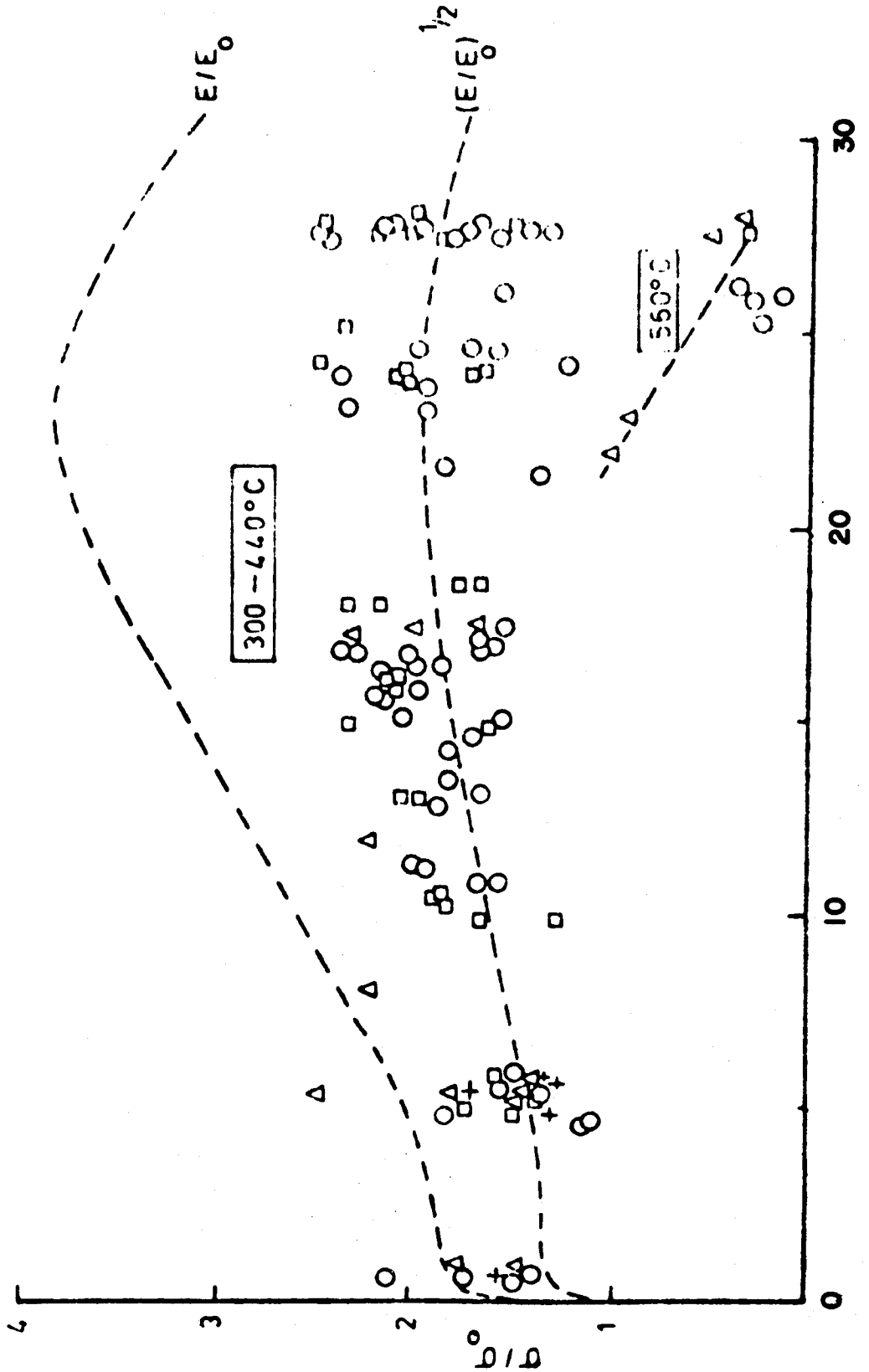

Fig. 15 --- Tensile Strength Changes with Fast-Neutron Dose for different Near-Isotropic Graphite Irradiated in DFR at 300 to 400°C and at 560°C.

well as γ are independent of the changes produced by radiation damage, then Eq. (15) reduces to

$$\sigma/\sigma_0 = \sqrt{E/E_0} \tag{16}$$

where σ_0 and E_0 are the tensile stength and elastic modulus, respectively, before irradiation.

By using this relationship (16), the tensile strength can be computed, knowing the elastic modulus. The latter, in turn, can be related to the porosity of the graphite. Although an exact relationship between elastic properties and porosity can only be established if the porosity is characterized in great detail, approximate relationships have been derived by many authors. These relationships give both upper and lower bounds for the elastic moduli as a function of the volume fraction of the porosity. In our analysis, we have used the results of Christensen,[11] who gives as a lower bound for the shear modulus the expression

$$\frac{G}{G^*} = \left\{1 + \frac{15(1-\nu)(7+5\nu)(p^{7/3}-1)p}{(7-5\nu)(7+5\nu)(1-p)(p^{7/3}-1)+126p(1-p^{2/3})^2}\right\}^{-1} \tag{17}$$

Here, ν is Poisson's ratio, G* the shear modulus of the theoretically dense material, and p is the volume fraction of the pores, i.e. p = P/100. In order to compute a lower bound for E/E*, it would be necessary to utilize the lower bound for the ratio K/K* for the bulk modulus, which was also given by Christensen.[11] However, since G is much more affected by the porosity than K, we use the approximation

$$\frac{E}{E^*} \cong \frac{G}{G^*} ,$$

and we replace the relationship in Eq. (16) by

$$\frac{\sigma}{\sigma_o} \cong \sqrt{\frac{G}{G_o}} = \sqrt{\frac{G}{G^*}\frac{G^*}{G_o}} , \tag{18}$$

where G_o/G^* is given by Eq. (17) for $p = P_o/100$. The degradation of the tensile strength of graphite can now be computed with the help of Eqs. (18), (17), and Eq. (3).

II.5 Fatigue Strength of Graphite

When graphite is subjected to alternating loads, fatigue fracture occurs at stress levels below the static strength of the material. In general, the lower the stress amplitude produced by the alternating load, the greater is the number of load cycles the material can endure before fracture.

Due to the heterogeneous structure of graphite, static as well as fatigue strengths show large statistical variations from sample to sample. As an example, Fig. shows[10] the data for tensile fatigue (i.e. the alternating stress varies between zero and $\sigma_a > 0$). The data points represent the homologous stress $s_h = \sigma_a/\bar{\sigma}_s$, where $\bar{\sigma}_s$ is the average value of the static tensile strength. A substantial reduction of the data scatter can be achieved if the homologous stress is defined as $\sigma_h = \sigma_a/\sigma_s$, where σ_s is now a statistically defined value of the fracture strength during the first cycle which is analyzed according to a Weibull distribution.

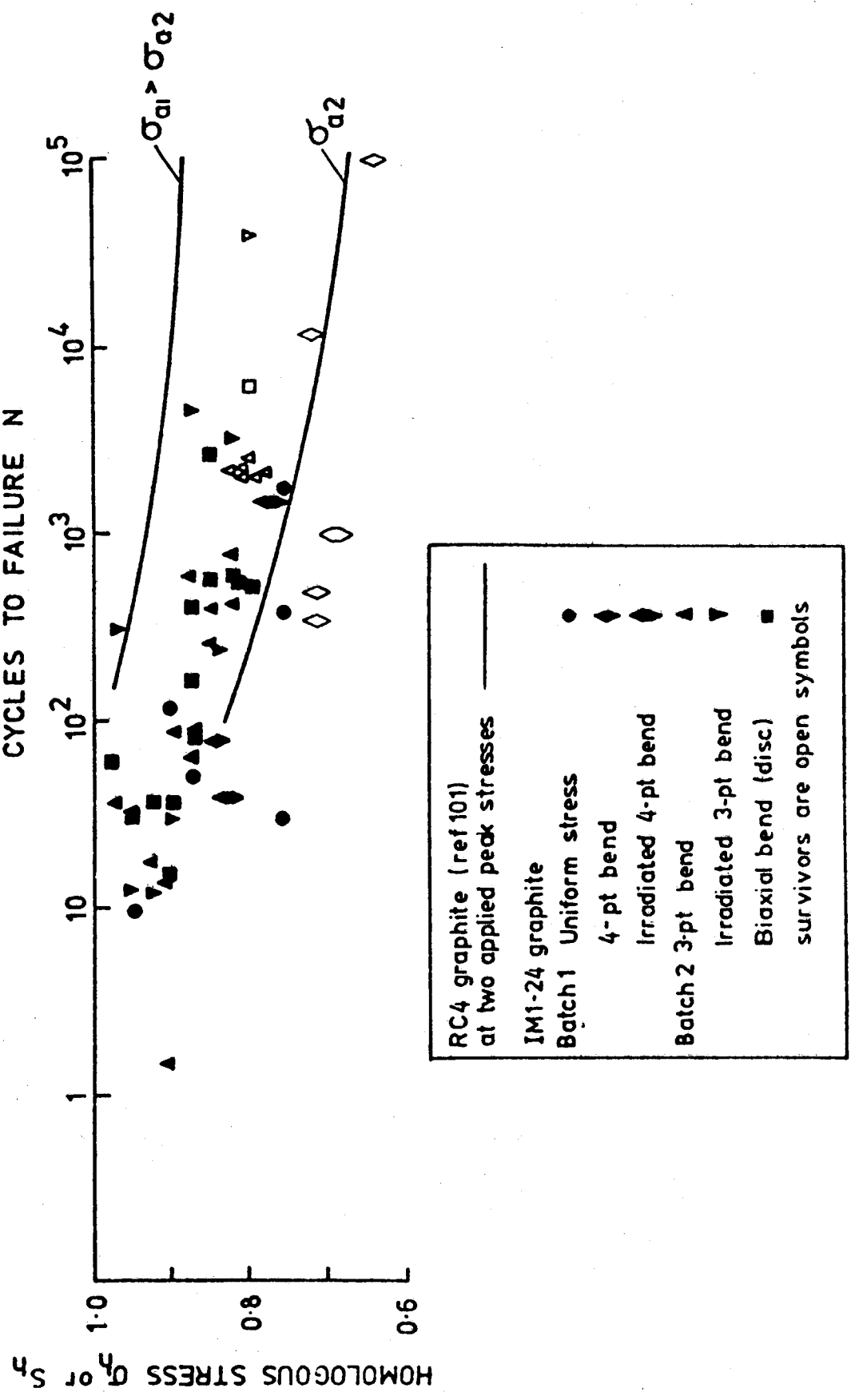

Fig. 16 -- Fatigue Endurance Data for Various Graphites under Tensile Fatigue Loading

Fatigue curves based on σ_h are shown in Fig. 16 as solid curves.

Regardless of the definition of the homologous stress, however, it is seen that a long fatigue life can be obtained if the stress amplitude does not exceed 65% of the static strength.

It is necessary to modify this rule somewhat since the fatigue life depends also on the mean stress. This is demonstrated by Fig. 17 which shows the fatigue curves for a mean stress of $\sigma_a/2$ (tensile fatigue) and for zero mean stress (loading between $+\sigma_a/2$ and $-\sigma_a/2$). Accordingly, it appears to be prudent to adopt the conservative rule that the tensile stress level for fatigue loading should not exceed one-half of the static tensile strength. This rule has been employed in the following stress analysis of the blanket structure as a design criterion.

III. Stress and Failure Analysis of the Blanket

III.1- Procedure for Lifetime Analysis

A lifetime analysis of the blanket structure was carried out according to the following guidelines, illustrated by the flow-diagram in Fig.

The central criterion for determining the lifetime was that the stress at any location in the blanket structure must be lower than one-half of the tensile strength at that location. This must be true for the stress distribution during reactor operation as well as during a shutdown.

To implement this procedure, it is necessary to first specify the boundary conditions and the distribution of temperature and atomic displacement rates. Next, the thermal stress distribution is computed, and

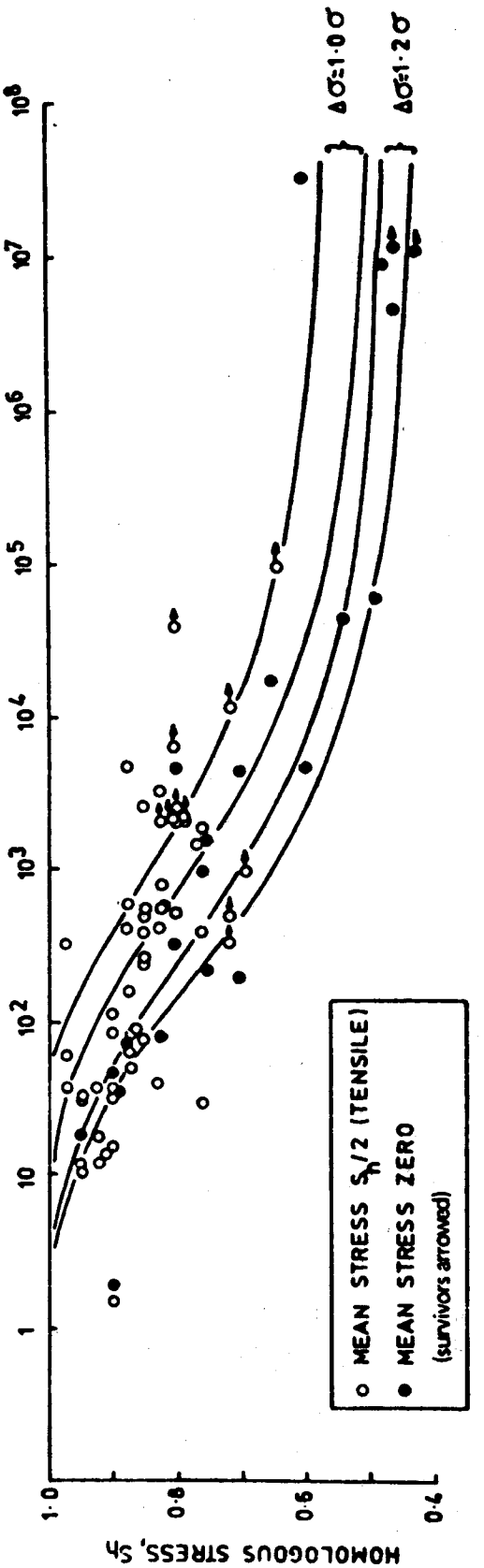

Fig. 17 -- Comparison of Fatigue Endurance Data for Tensile Fatigue (open symbols) and for Fatigue with zero mean stress (solid symbols)

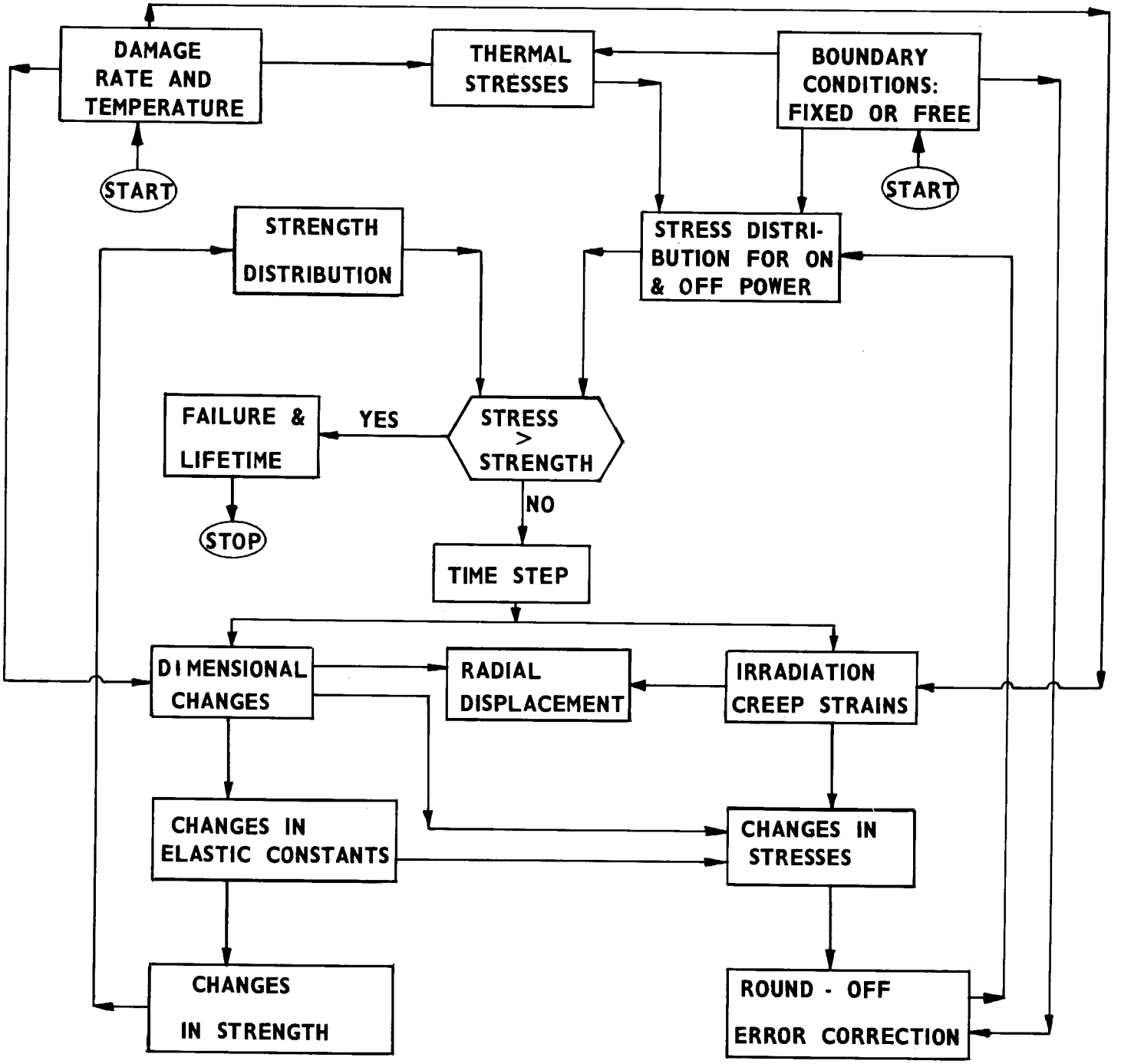
DAMAGE RATE AND TEMPERATURE
START
THERMAL STRESSES
BOUNDARY CONDITIONS: FIXED OR FREE
START
STRENGTH DISTRIBUTION
STRESS DISTRI-BUTION FOR ON & OFF POWER
FAILURE & LIFETIME
YES
STRESS > STRENGTH
NO
STOP
TIME STEP
DIMENSIONAL CHANGES
RADIAL DISPLACEMENT
IRRADIATION CREEP STRAINS
CHANGES IN ELASTIC CONSTANTS
CHANGES IN STRESSES
CHANGES IN STRENGTH
ROUND - OFF ERROR CORRECTION

FIGURE 18

it is tested whether the strength is exceeded. Then, for a short time step, the change of the porosity, elastic modulus, and static strength is calculated. In addition, the irradiation creep strains are computed for this time interval, and the new stress distributions for on and off power are evaluated. Comparison between stresses and strength is made again. This cycle is repeated until the failure criterion is satisfied at some location in the blanket structure.

This procedure represents a general, self-consistent approach to the determination of the lifetime of fusion reactor components. However, to carry it out in detail would have required an inelastic finite-element analysis which was judged to be beyond the scope of this design study. Therefore, we selected a part of the blanket structure for the analysis which is subject to the largest temperature and neutron flux gradients. Clearly, this part is one of the radial dividers in a blanket module. To further simplify the analysis the radial divider was modelled as a thin, annular disk as illustrated in Fig. 19. This simulated in an approximate fashion the circumferential constraints imposed on the blanket sections when they are connected to form the entire reactor cavity.

III.2 Inelastic Stress Analysis

In this section, we describe briefly the inelastic analysis of the blanket radial divider modelled as an annular disk.[12] The reader interested only in the final results may wish to proceed to the next section.

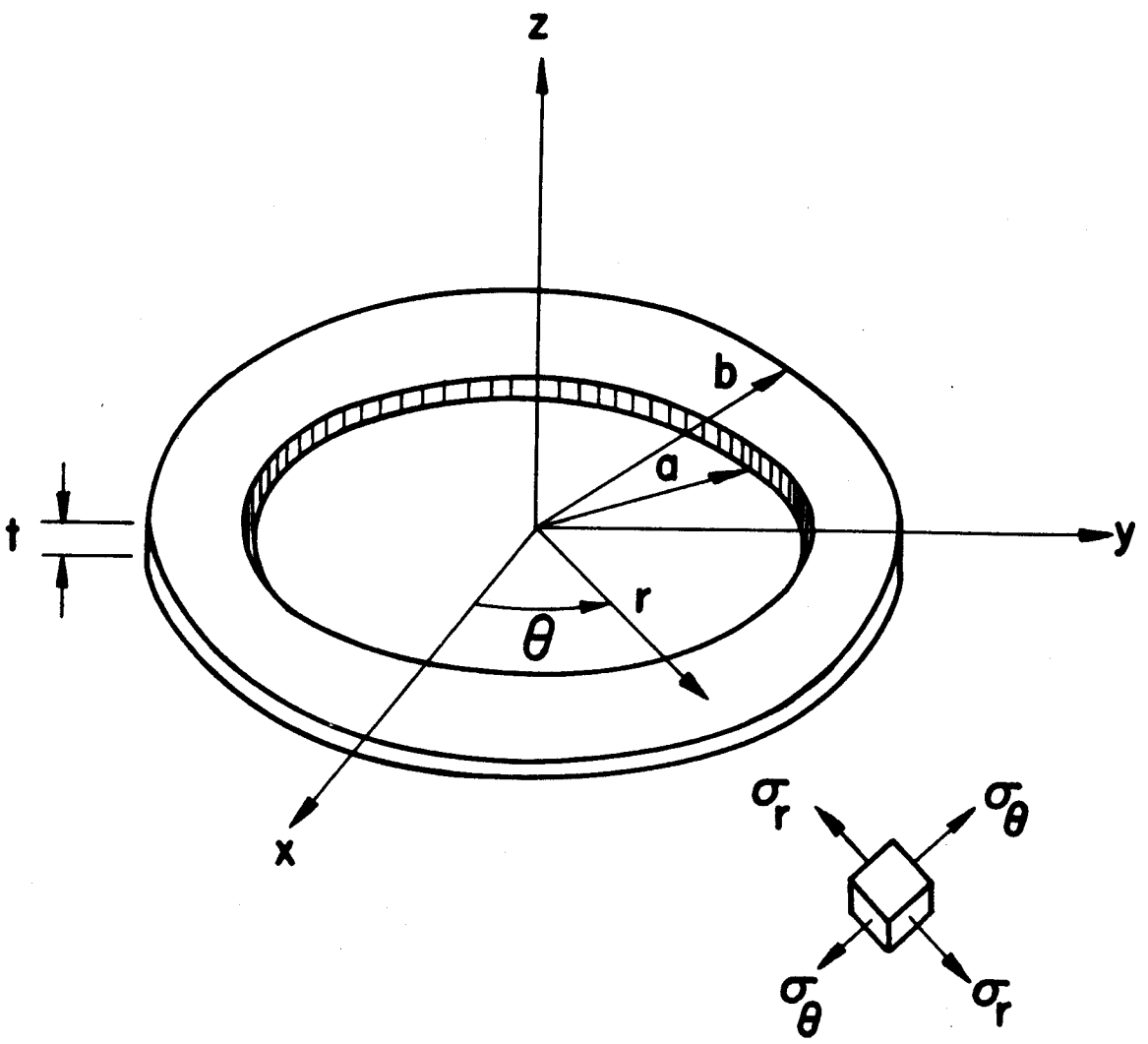

a = 6.0 meters
b = 6.6 meters
t = 0.64 centimeters

Fig. 19 -- Blanket Radial Divider Modelled as an Annular Disk, and Loaded in Plane Stress

If we neglect the circumferential variation of the temperature, i.e. assume axial symmetry, then the radial stress, σ_r, and the hoop stress, σ_θ, satisfy the equilibrium equation[12]

$$\frac{d\sigma_r}{dr} + \frac{\sigma_r - \sigma_\theta}{r} = 0 \tag{19}$$

The stress component normal to the disk can be neglected, i.e. $\sigma_z = 0$. If ε denotes a total and e an inelastic strain component, then Hooke's law is given by

$$\sigma_r = \frac{E}{1-\nu^2} \{(\varepsilon_r - e_r) + \nu (\varepsilon_\theta - e_\theta)\} \tag{20}$$

$$\sigma_\theta = \frac{E}{1-\nu^2} \{(\varepsilon_\theta - e_\theta) + \nu (\varepsilon_r - e_r)\} \tag{21}$$

The total strain components can be derived from a radial displacement function u(r) according to

$$\varepsilon_r = \frac{du}{dr}, \quad \varepsilon_\theta = \frac{u}{r} \tag{22}$$

If these equations are used in Eqs. (20) and (21), then Eq. (19) gives

$$\frac{d}{dr}\left(\frac{1}{r}\frac{d(ru)}{dr}\right) = \frac{d}{dr}(e_r + \nu e_\theta) + (1 - \nu)\frac{(e_r - e_\theta)}{r} \tag{23}$$

Integrating this equation twice we obtain after some manipulation the result

$$u(r) = \frac{1}{2} C_1 r + \frac{C_2}{r} + \frac{(1+\nu)}{2r} A(r) + \frac{(1-\nu)}{2} rB(r) \tag{24}$$

where

$$A(r) = \int_a^r r'dr' \ (e_r + e_\theta) \tag{25}$$

$$B(r) = \int_a^r \frac{dr'}{r'} \ (e_r - e_\theta) \tag{26}$$

The constants C_1 and C_2 must be determined from the boundary conditions. On the inner boundary, at $r = a = 6$ meters,

$$\sigma_r(a) = 0 \tag{27}$$

From Eqs. (24), (22), (20), and (21) one can derive the following expressions:

$$\frac{\sigma_r}{E} = \frac{C_1}{2(1-\nu)} - \frac{C_2}{(1+\nu)r^2} - \frac{A(r)}{2r^2} + \frac{1}{2} B(r) \tag{28}$$

$$\frac{\sigma_\theta}{E} = \frac{C_1}{2(1-\nu)} + \frac{C_2}{(1+\nu)r^2} + \frac{A(r)}{2r^2} + \frac{1}{2} B(r) - e_\theta \tag{29}$$

Hence, $\sigma_r(a) = 0$ implies that

$$\frac{C_1}{2(1-\nu)} = \frac{C_2}{(1+\nu)a^2} = C$$

and

$$\frac{\sigma_r}{E} = C \ (1 - \frac{a^2}{r^2}) - \frac{A(r)}{2r^2} + \frac{1}{2} B(r) \tag{30}$$

$$\frac{\sigma_\theta}{E} = C\left(1 + \frac{a^2}{r^2}\right) + \frac{A(r)}{2r^2} + \frac{1}{2}B(r) = e_\theta \tag{31}$$

For the condition at the outer boundary, namely at r = b = 6.6 m, we can consider either a stress-free situation, i.e.

$$\sigma_r(b) = 0$$

or a rigid constraint, i.e.

$$u(b) = 0$$

For the stress-free case,

$$C = \frac{A(b)}{2(b^2-a^2)} - \frac{b^2B(b)}{2(b^2-a^2)} \tag{32}$$

and for the rigid boundary,

$$C = \frac{-(1+\nu)A(b)+(1-\nu)b^2B(b)}{2[(1-\nu)b^2+(1+\nu)a^2]} \tag{33}$$

If the inelastic strains e_r and e_θ are known, the functions A(r) and B(r) can be computed, C be determined from either Eq. (32) or (33), and the stresses can then be found from Eqs. (30) and (31). For the initial thermal stresses, $e_r = e_\theta = \alpha(r)T(r)$ where α is the linear thermal expansion coefficient. To compute the time dependence of the stresses as a consequence of irradiation creep we differentiate Eqs. (30) and (31) with respect to time, holding a and b constant. The differentiation of A(r)

and B(r) results in the appearance of the inelastic strain rates $\dot{e}_r$ and $\dot{e}_\theta$. For isotropic graphite these strain rates are given by

$$\frac{de_r}{dt} = \dot{e}_r = \frac{1}{3}\dot{P} + (KE\dot{F})\left[\sigma_r - \frac{1}{2}\sigma_\theta\right]\frac{1}{E} \tag{34}$$

$$\frac{de_\theta}{dt} = \dot{e}_\theta = \frac{1}{3}\dot{P} + (KE\dot{F})\left[\sigma_\theta - \frac{1}{2}\sigma_r\right]\frac{1}{E} \tag{35}$$

where $\dot{P}$ can be obtained from Eq. (3). The irradiation creep coefficient KE is given by Eq. (14). Substituting these equations into the expressions for $\dot{A}$ and $\dot{B}$ we obtain

$$\dot{A}(r) = \frac{2}{3}\int_a^r r\,dr\dot{P} + \frac{1}{2}\int_a^r r\,dr\; KE\dot{F}\left(\frac{\sigma_r}{E} + \frac{\sigma_\theta}{E}\right) \tag{36}$$

$$\dot{B}(r) = \frac{3}{2}\int_a^r \frac{dr}{r}\; KE\dot{F}\left(\frac{\sigma_r}{E} - \frac{\sigma_\theta}{E}\right) \tag{37}$$

The rate of change for the stresses is given by

$$\frac{d}{dt}\left(\frac{\sigma_r}{E}\right) = \dot{C}\left(1 - \frac{a^2}{r^2}\right) - \frac{\dot{A}(r)}{2r^2} + \frac{1}{2}\dot{B}(r) \tag{38}$$

$$\frac{d}{dt}\left(\frac{\sigma_\theta}{E}\right) = \dot{C}\left(1 + \frac{a^2}{r^2}\right) + \frac{\dot{A}(r)}{2r^2} + \frac{1}{2}\dot{B}(r) - \frac{1}{3}\dot{P} - KE\dot{F}\left(\frac{\sigma_r}{E} - \frac{\sigma_\theta}{2E}\right) \tag{39}$$

We note that by making the assumption that the irradiation creep constant (KE) is independent of the dose, the changing modulus can be easily accommodated in the stress analysis. In view of the large scatter of the irradiation creep data this assumption is just as good as the original one (namely a constant coefficient KE_0, where E_0 is the initial Young's modulus).

The two equations (38) and (39) represents a coupled set of integro-differential equations. The integral expressions for $\dot{A}$ and $\dot{B}$ were evaluated with the trapezoidal rule, and the Eqs. (38) and (39) are then replaced by a set of first order ordinary differential equations for the stresses at the nodal points, r_i. This set of equations was then intregated numerically by using a finite difference scheme with respect to time. Using a forward time step method, we get:

$$\dot{\sigma}_r(r,t) \cong \frac{[\sigma_r(r,t+\Delta t) - \sigma_r(r,t)]}{\Delta t} \tag{40}$$

Therefore:

$$\sigma_r(r,t+\Delta t) \simeq \Delta t\dot{\sigma}_r(r,t) + \sigma_r(r,t) \tag{41}$$

where Δt = time step.

Although the numerical integration as outlined at the beginning of this section is straightforward, it was found that numerical errors accumulated rapidly unless the following corrections were applied after each time step. Integration of the equation (19) yields

$$\int_a^b \sigma_\theta(r)dr = b\sigma_r(b) \tag{42}$$

which is applicable for both free or fixed outer boundary conditions. Because the stresses are computed only at a finite number of points, the corresponding relationship

$$\sum_i \sigma_\theta(r_i)\Delta r_i - b\sigma_r(b) = R \tag{43}$$

will yield equilibrium only when the residual R = 0. It was found that this residual R is quite small for each individual time step, but can accumulate quite rapidly. Therefore, after each time step, the nodal stresses $\sigma_\theta(r_i)$ were corrected by addition of the term R/(b-a). The values for σ_θ and σ_r are forced to satisfy Eq. (40), so that R = 0.

Because of the large strains that accumulate over the entire lifetime, the radial positions, r_i, were corrected after each time step by adding the incremental displacement $\dot{u}(r_i)\Delta t$ of each nodal point to the previous nodal radius r_i. Here, $\dot{u}\Delta t$ was computed with Eq. (24). A finite strain analysis was accomplished in this fashion, and the radial motion of the disk could be followed.

III.3 Results of the Stress Analysis

The inelastic stress analysis was carried out with 14 nodal points, whose position was selected to closely match the temperature profile. Table 3 lists the location of these nodal points together with the corresponding temperatures and radiation damage rates. It is seen that the temperature drops off precipitously over the first two centimeters and remains essentially constant for the remainder of the divider in the radial direction. The dose rate, on the other hand, decreases more uniformly across the blanket thickness, as illustrated in Fig. 20.

The computations of all stresses were carried out in the dimensionless units (σ/E_0), where E_0 is the Young's modulus of the unirradiated graphite. For the purpose of representation, however, the nodal stresses and strength are given in units of ksi which were obtained from the dimensionless values by multiplying them with $E_0 = 10^6$ psi. It should be noted that the comparison of strength and stress is independent of the values chosen for E_0.

The other materials parameters that were selected as input data for the computation were Poisson's ratio $\nu = 0.2$ and the linear thermal expansion coefficient of $\alpha = 4 \times 10^{-6}/^{o}K$.

Table 3

Initial Nodal Points with Corresponding Temperatures and Damage Rates

Nodal Points (m)	Temperature (°C)	Damage Rate (dpa/yr)
6.000	1500	32.50
6.003	1220	32.28
6.006	1050	32.10
6.01	886	31.75
6.02	688	31.00
6.03	625	30.25
6.04	607	29.50
6.06	602	28.00
6.10	600	25.00
6.20	600	17.50
6.30	600	12.00
6.40	600	6.5
6.50	600	3.93
6.60	600	1.35

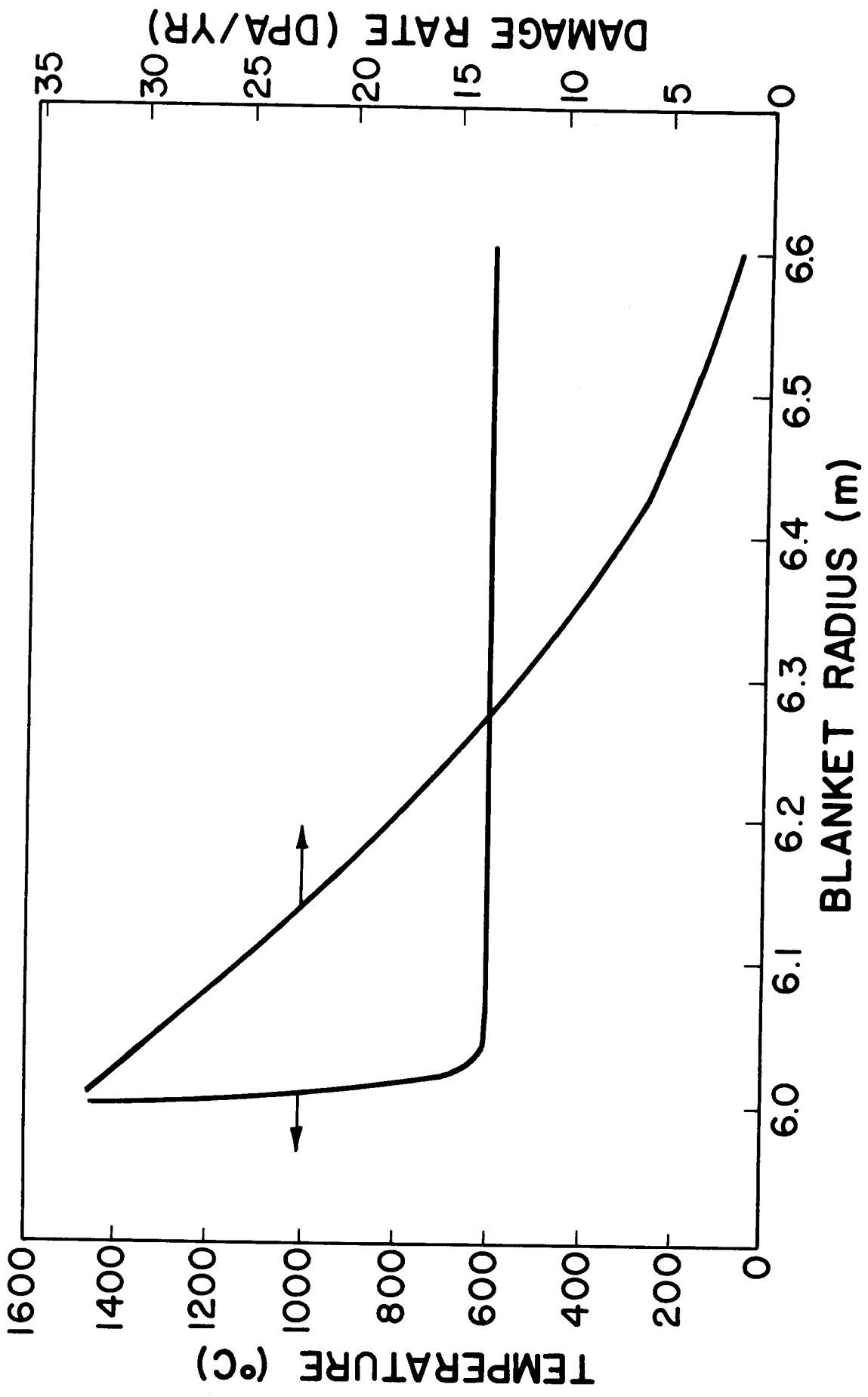
DAMAGE RATE (DPA/YR)
35
30
25
20
15
10
5
0
6.0
6.1
6.2
6.3
6.4
6.5
6.6
BLANKET RADIUS (m)
1600
1400
1200
1000
800
600
400
200
0
TEMPERATURE (°C)

FIGURE 20

The sequence of Figs. 21 to 29 shows the radial distribution of the hoop stress σ_θ for on and off power together with the distribution of one-half of the tensile strength for a graphite with 5% initial porosity.

It was assumed that the densification is described by the nominal case of Eq. (9), and that the final growth rate is the one given by Eq. (8) for low-growth graphites. Furthermore, the stress-free boundary condition was selected for this example. Beginning with Fig. 21, the initial thermal stress distribution is shown. Because of irradiation creep, the thermal stresses relax rapidly, as can be seen from Figs. 22 and 23. After about a month of operation, densification of the graphite commences where the temperature and neutron flux is high. This gives rise to a small tensile stress on power at the inside of the disk, as seen in Fig. 24. Further irradiation leads then to expansion, particularly at the radial location $r \cong 6.01$ m, where the temperature is around $1000^{o}C$, the range of maximum expansion. At this location, compressive stresses build up, as seen in Fig. 25.

The increase in porosity at this location is reflected in the reduction of the strength. This degradation of the strength becomes more pronounced with irradiation, as illustrated by Figs. 26 to 29. It is seen that after about one year of operation the hoop stress for the off-power case approaches the value of 1/2 of the tensile strength near the inner boundary. It is important to emphasize that the analysis presented here shows that the stresses during shutdown are the controlling factor rather than the stresses during operation.

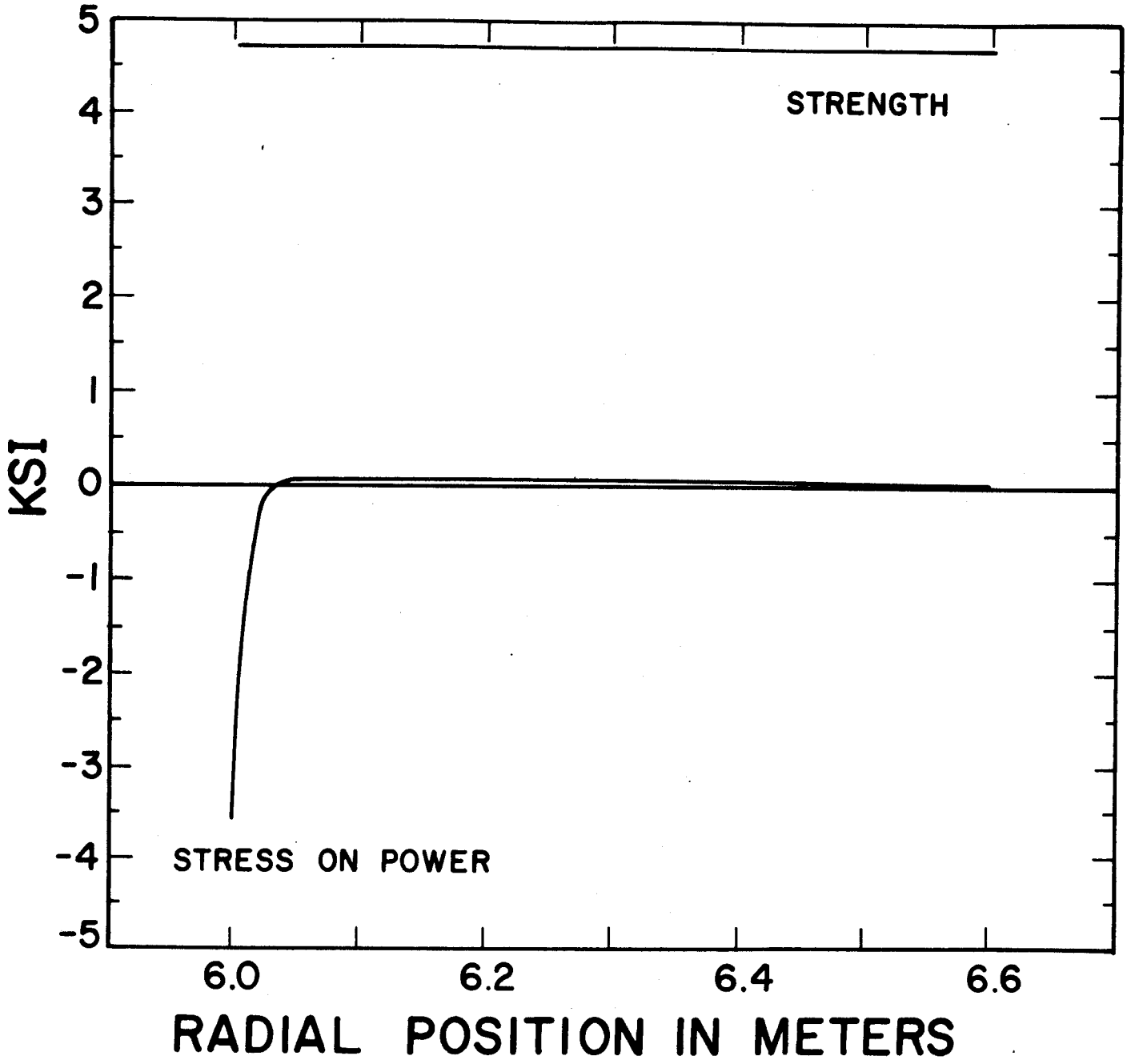

Fig. 21 Hoop Stress and Tensile Strength Distribution in the Radial Divider made of Low-Growth Graphite with 5% Initial Porosity; After Start-up

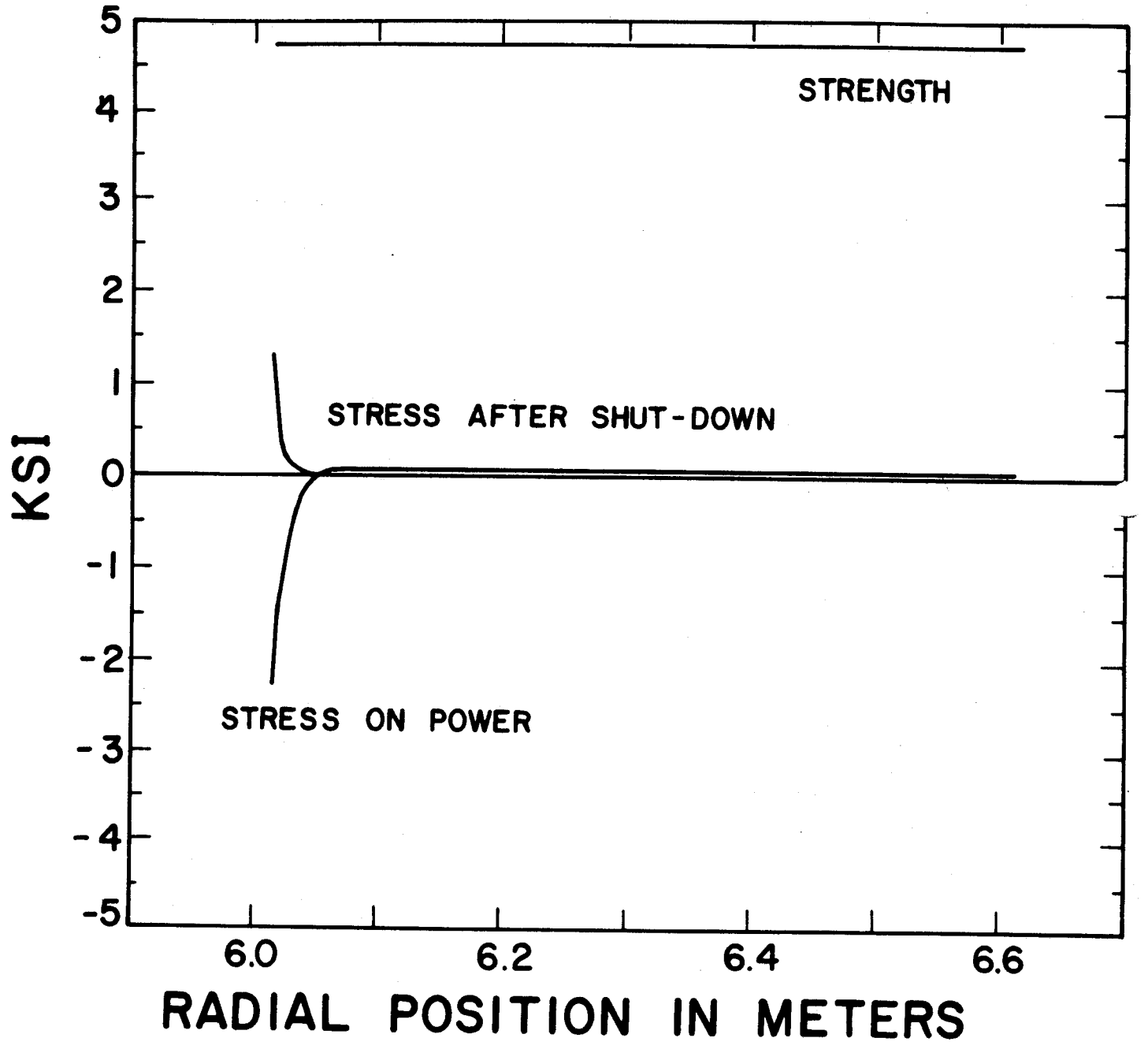

Fig. 22 ---- After 17.5 Hours of Irradiation

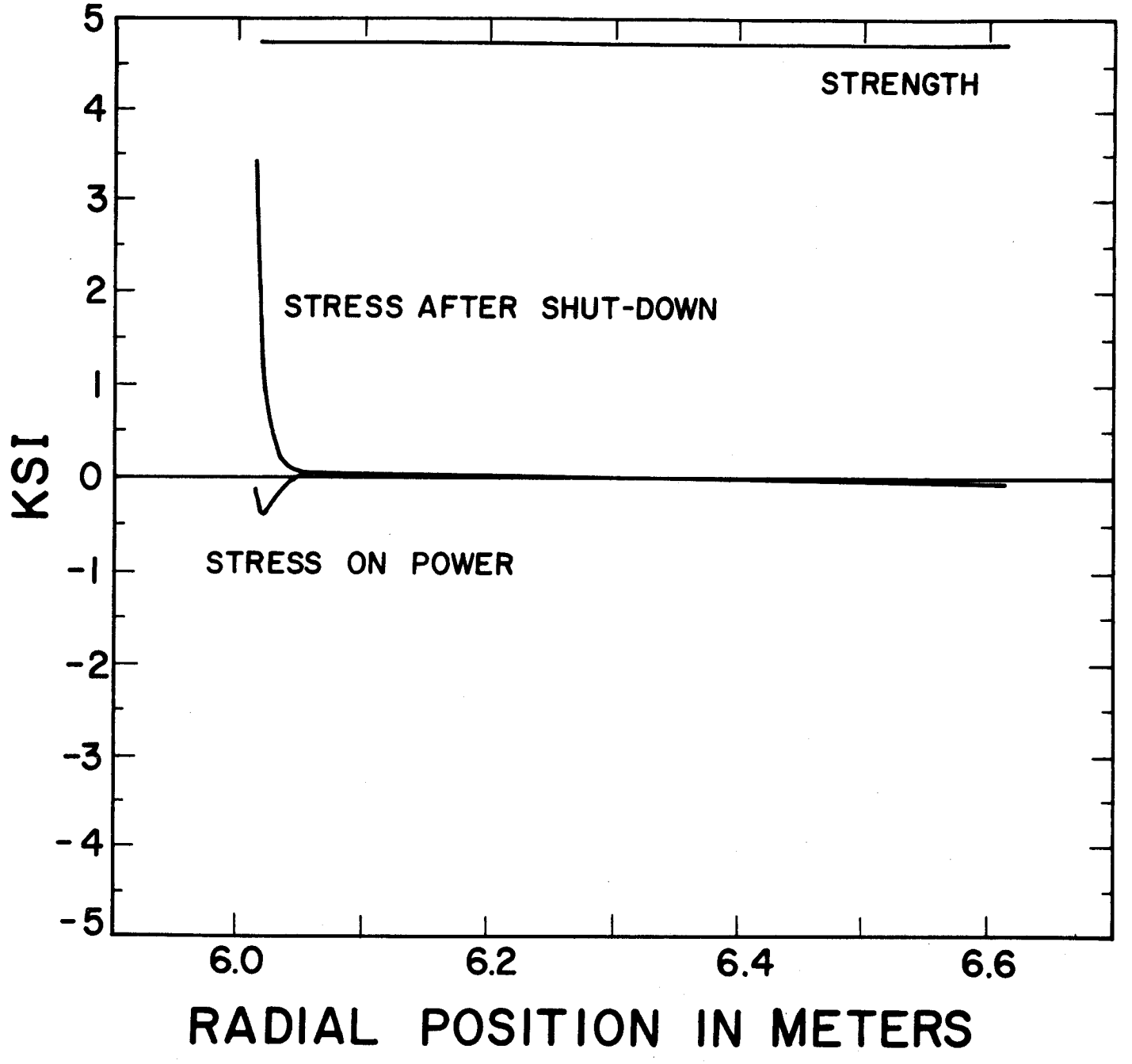

Fig. 23 -- After 3.6 Days of Irradiation

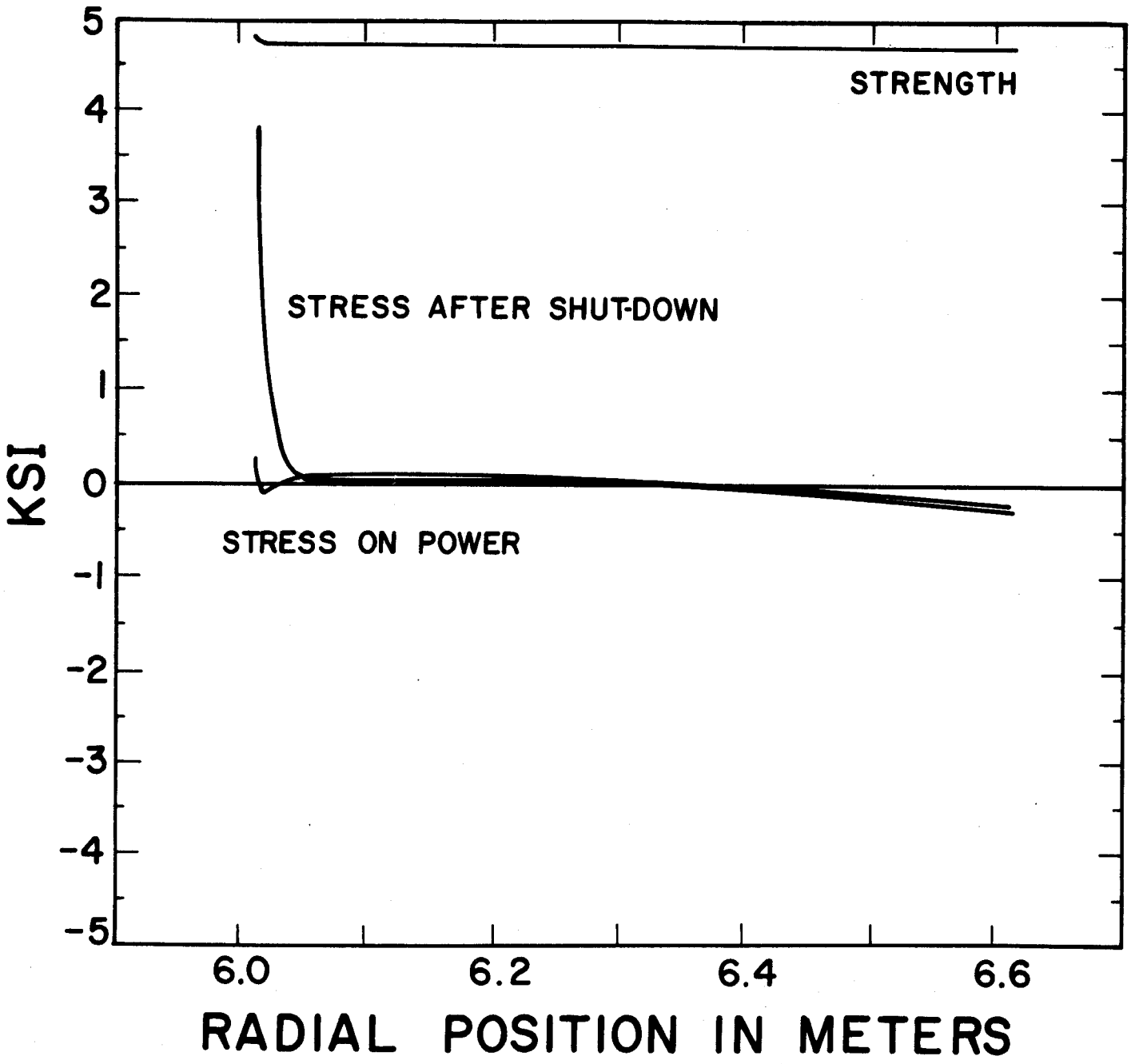

Fig. 24 -- After 36.5 Days of Irradiation

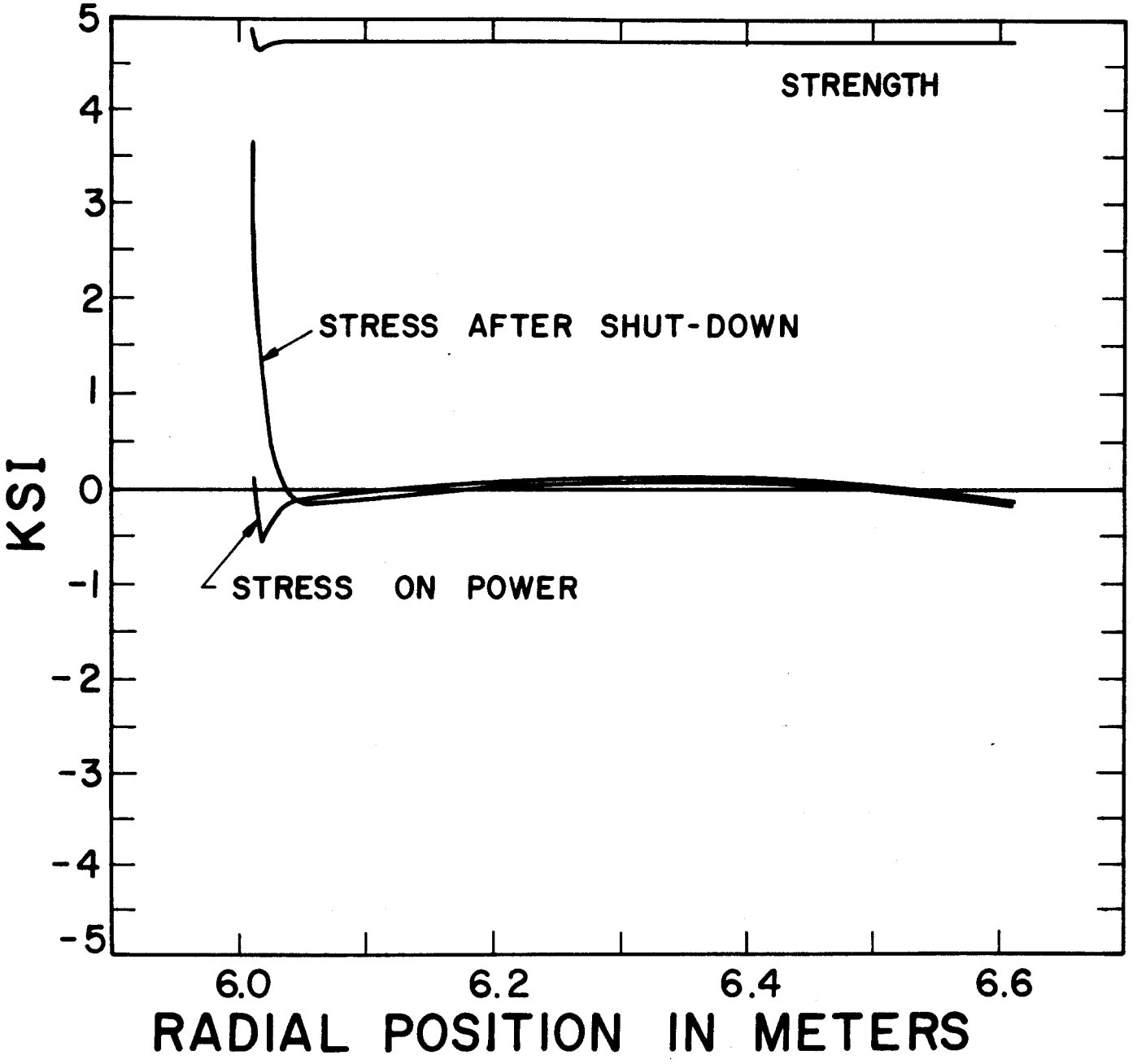

Fig. 25 -- After 0.2 Years of Irradiation

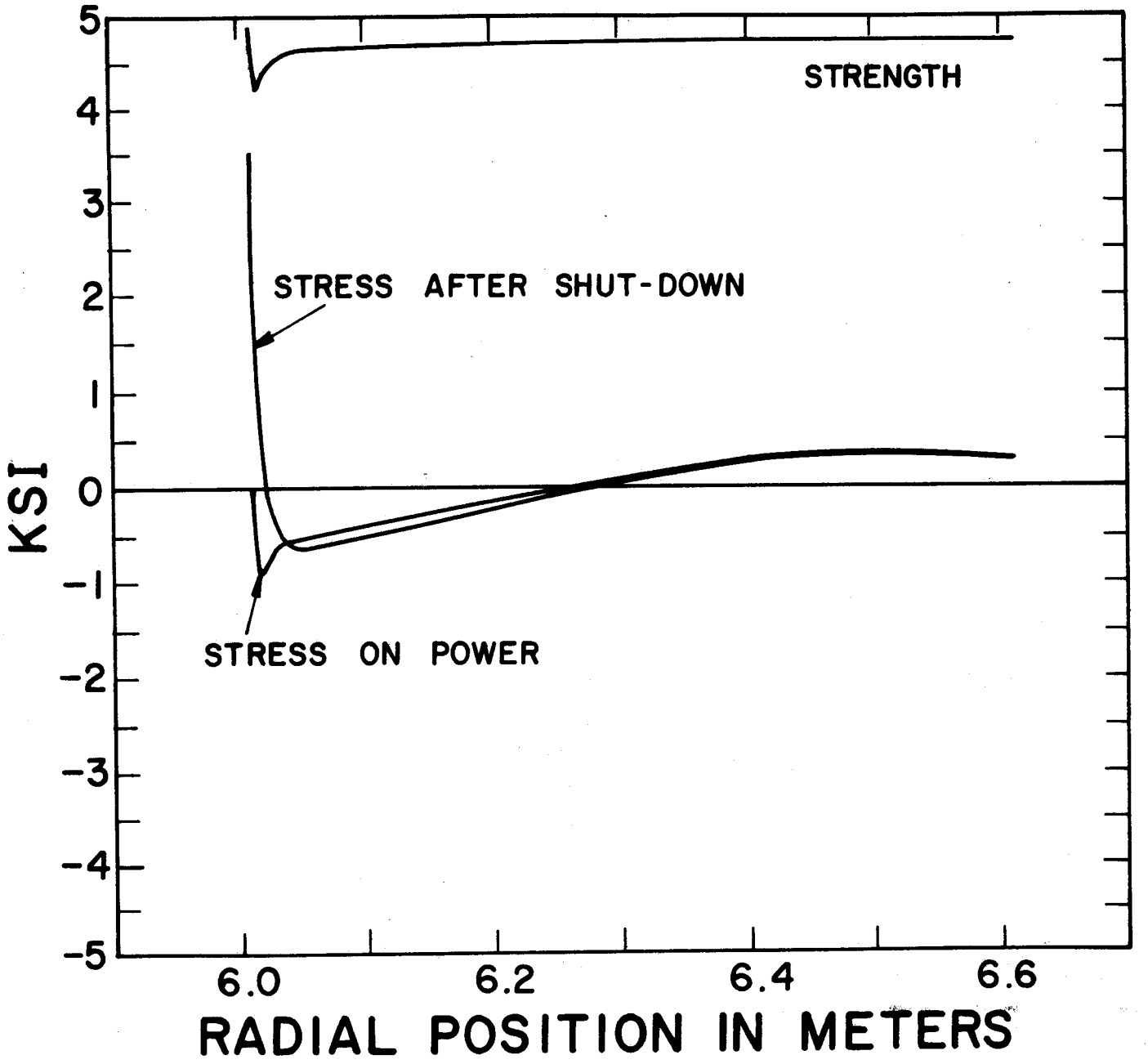

Fig. 26 -- After 0.4 Years of Irradiation

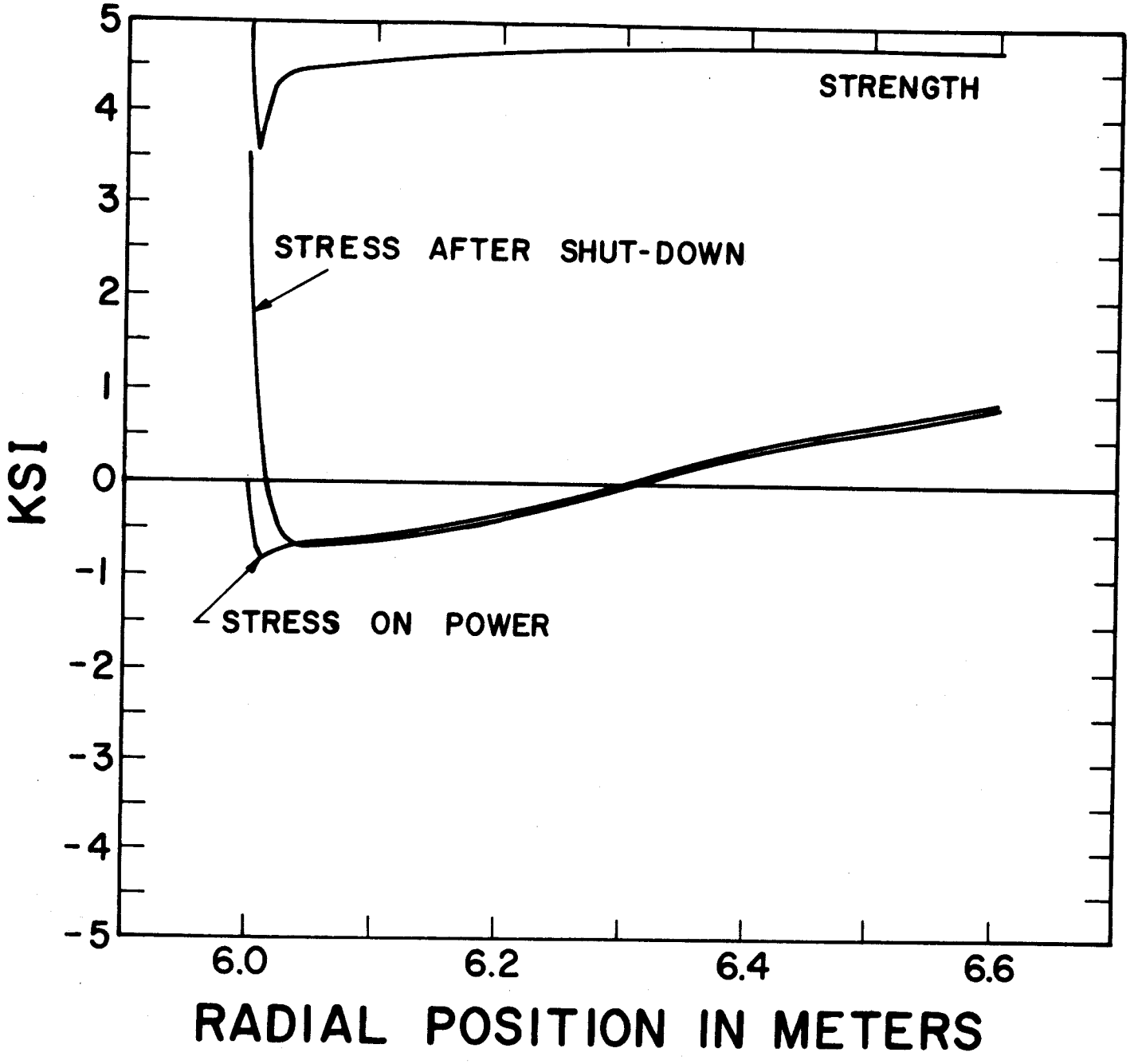

Fig. 27 -- After 0.6 Years of Irradiation

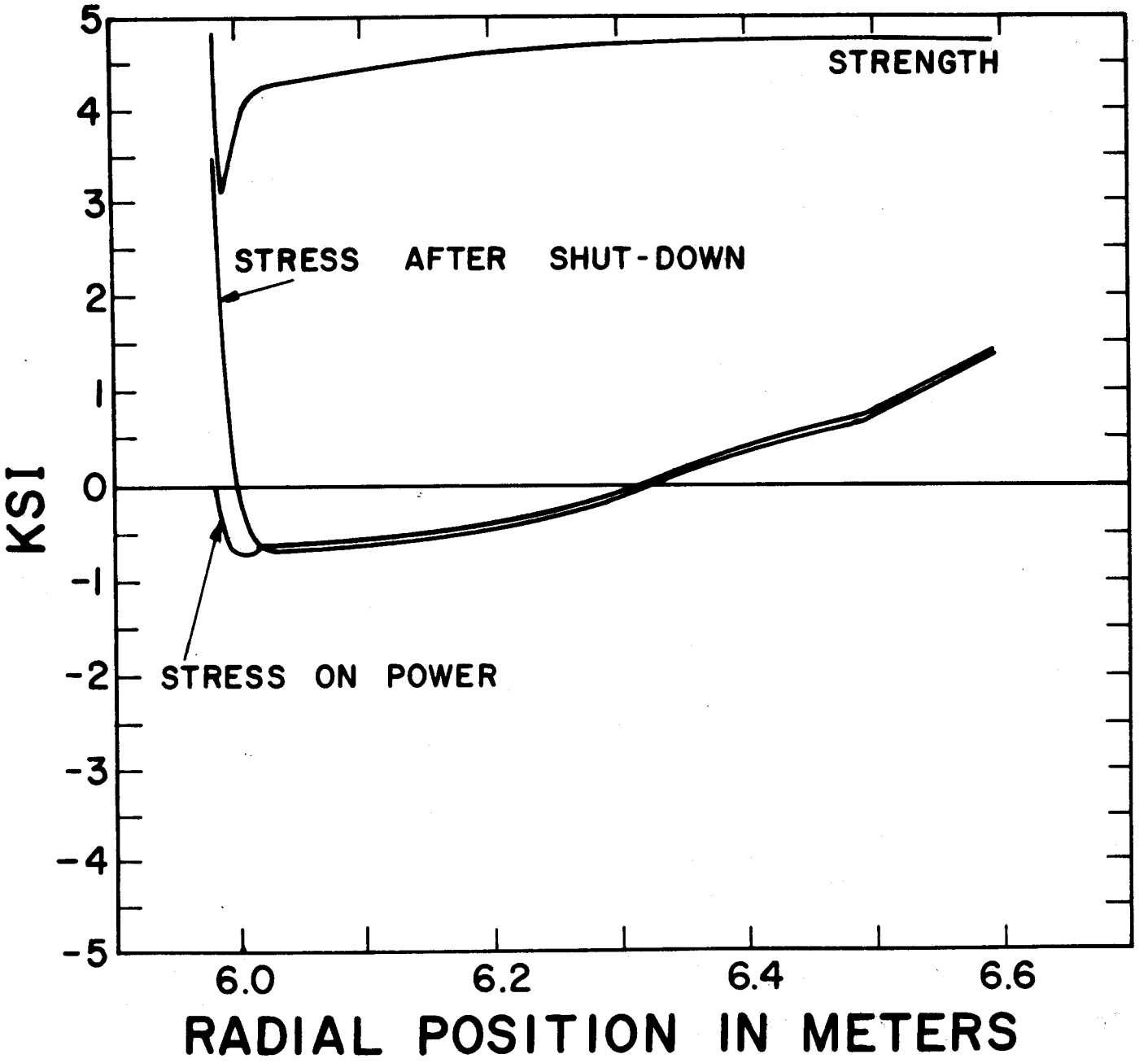

Fig. 28 -- After 0.8 Years of Irradiation

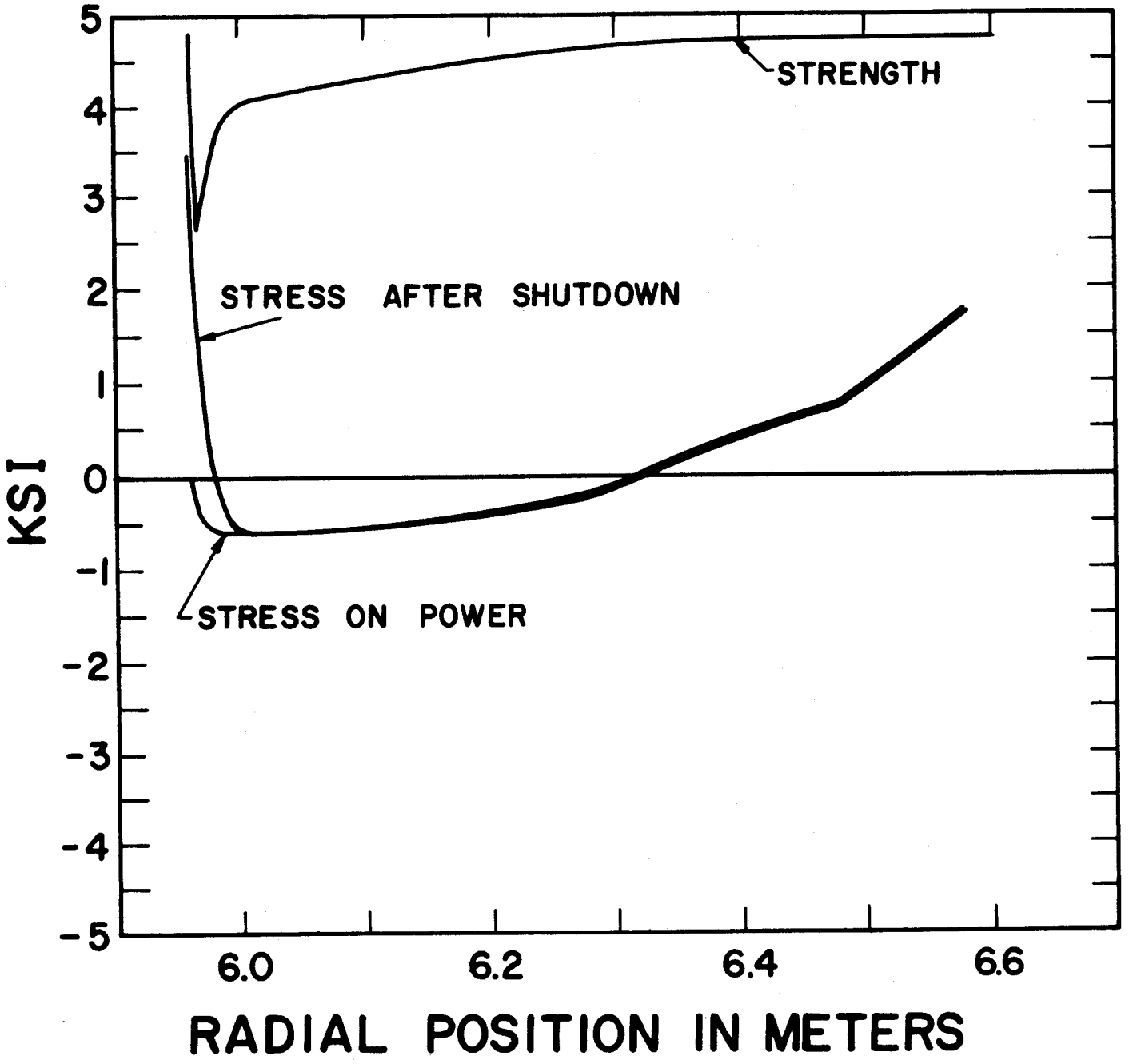

Fig. 29 -- After 1.0 Year of Irradiation

The case illustrated by the Figs. 21 to 29 is for a rather dense graphite with only 5% initial porosity. Present-day nuclear graphites have typically an initial porosity of 20%. For such a graphite material, the stress-distribution upon shutdown exceeds one-half of the strength after a short irradiation period of only 3.6 days. The reason for this situation, illustrated in Fig. 30 is that thermal stress relaxation and densification have produced a tensile hoop stress on the inner radius of the disk in excess of the safe limit. This problem persists up to an irradiation time of 36.5 days. At this time, the stresses are those shown in Fig. 31 and further irradiation removes the problem, as can be seen from Fig. 32 After about one year, the hoop stress near the inner boundary of the disk approaches again the value of 1/2 of the tensile strength, as shown in Fig. 33.

A similar calculation with a graphite of 10% initial porosity also showed that the stresses on shutdown after 3.6 days exceed the safe limit. However, in this case, the problem persisted only for an irradiation time of about 15 days.

If the computations were made with a dense high-growth graphite whose final volumetric expansion rate is given by Eq. (9), the lifetime was reduced to 0.4 years. Fig. 34 shows the stress and strength distribution for this case, assuming again a stress-free outer boundary.

Finally, we note that the stress-distribution in a graphite disk with fixed outer boundary, the thermal stresses already reach intolerable values at start-up. Therefore, it is important that the blanket structure is allowed to expand freely.

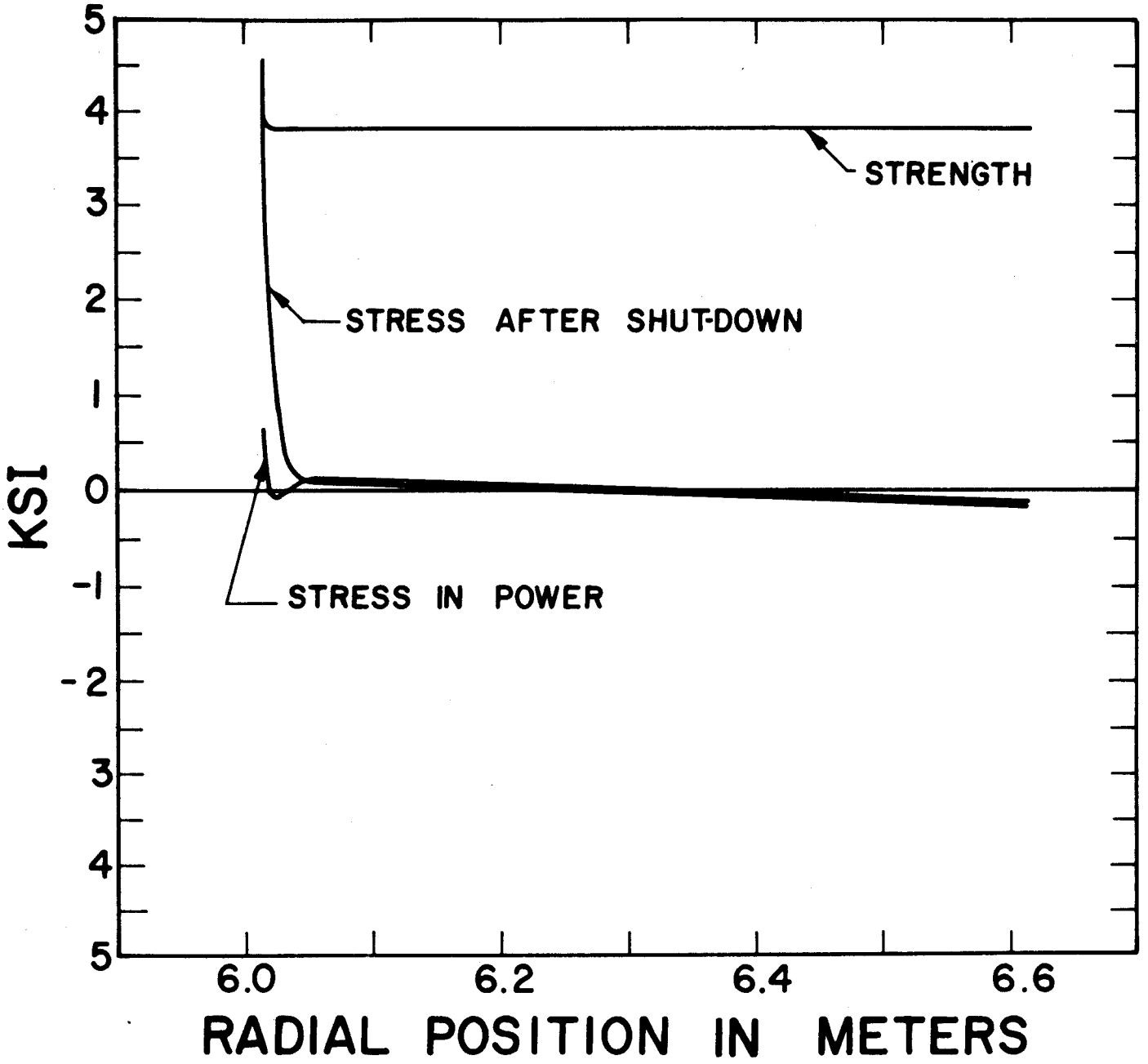

Fig. 30 Hoop Stress and Tensile Strength Distribution in the Radial Divider made of Low-Growth Graphite with 20% Initial Porosity; After 3.6 Days of Irradiation.

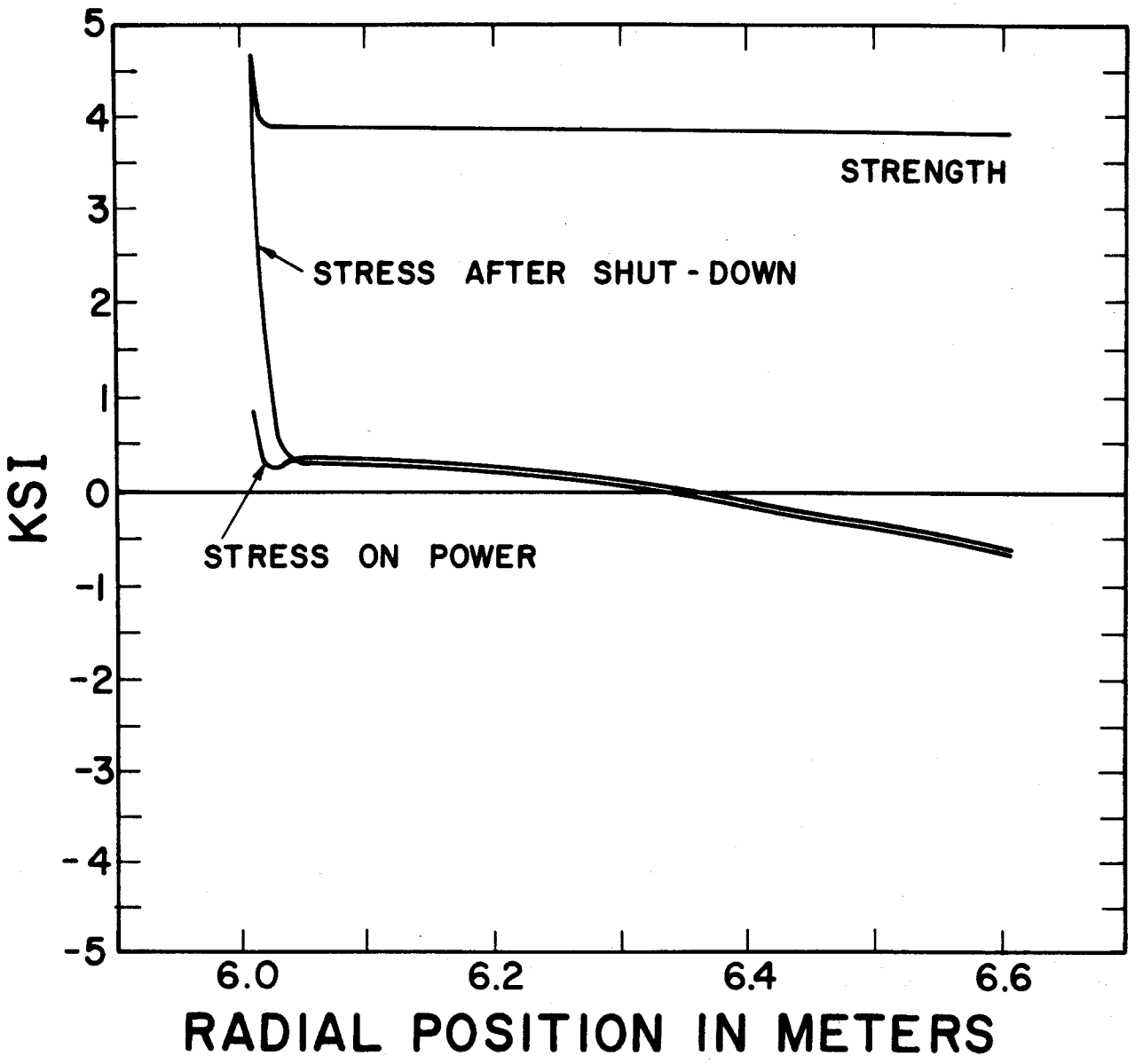

Fig.31 -- After 36.5 Days of Irradiation

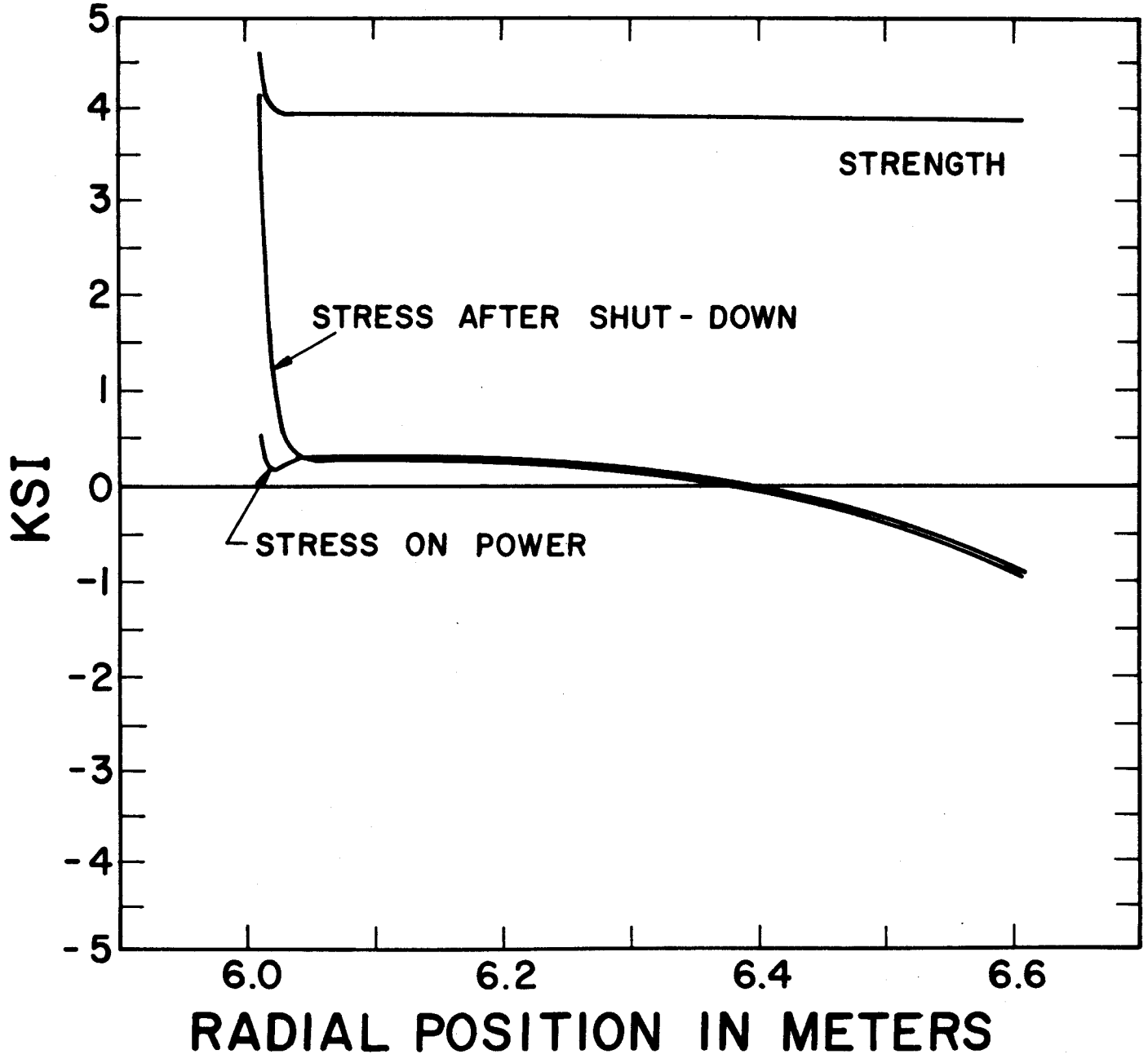

Fig. 32 -- After 73 Days of Irradiation

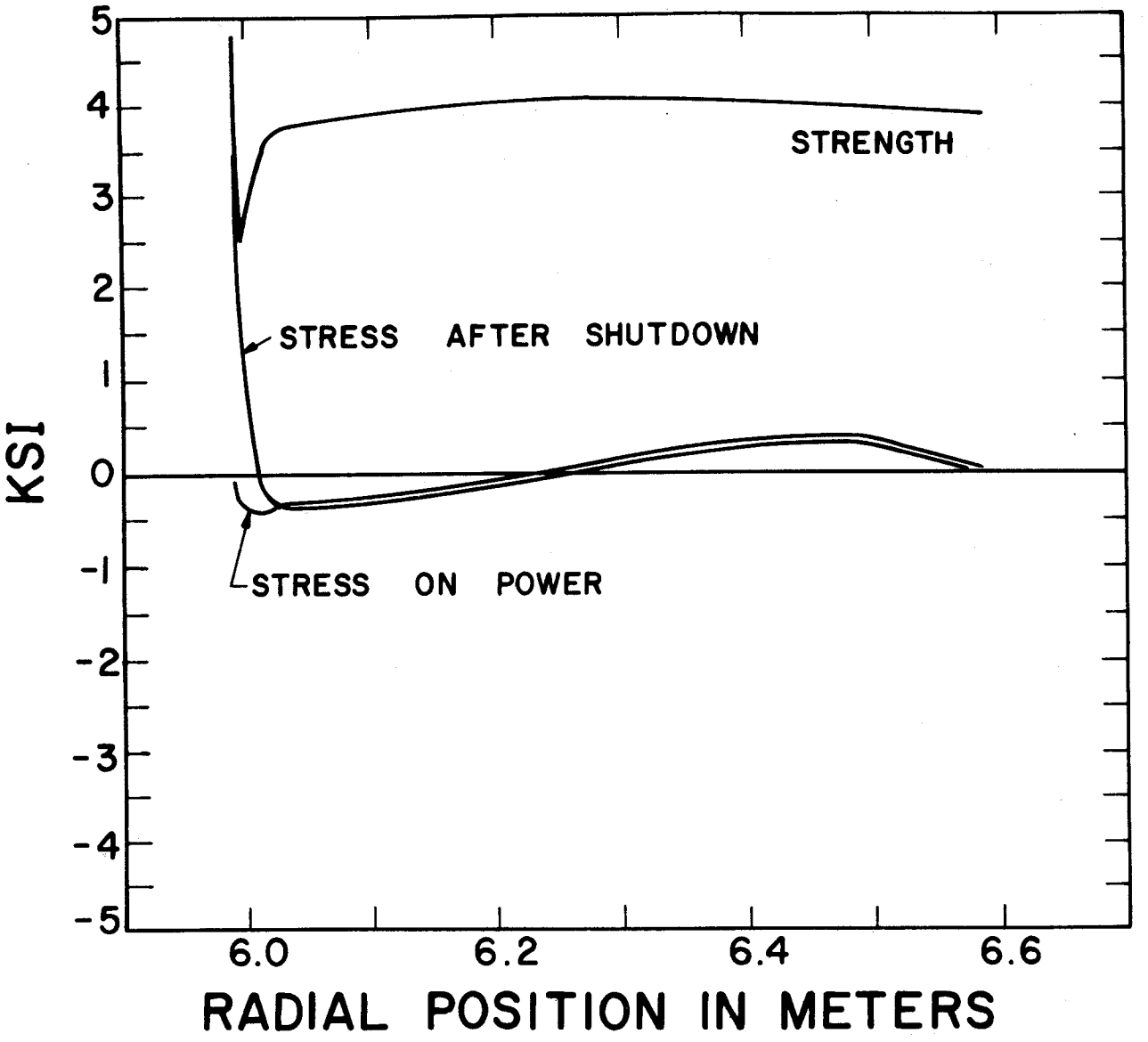

Fig. 33 After 1.2 Years of Irradiation

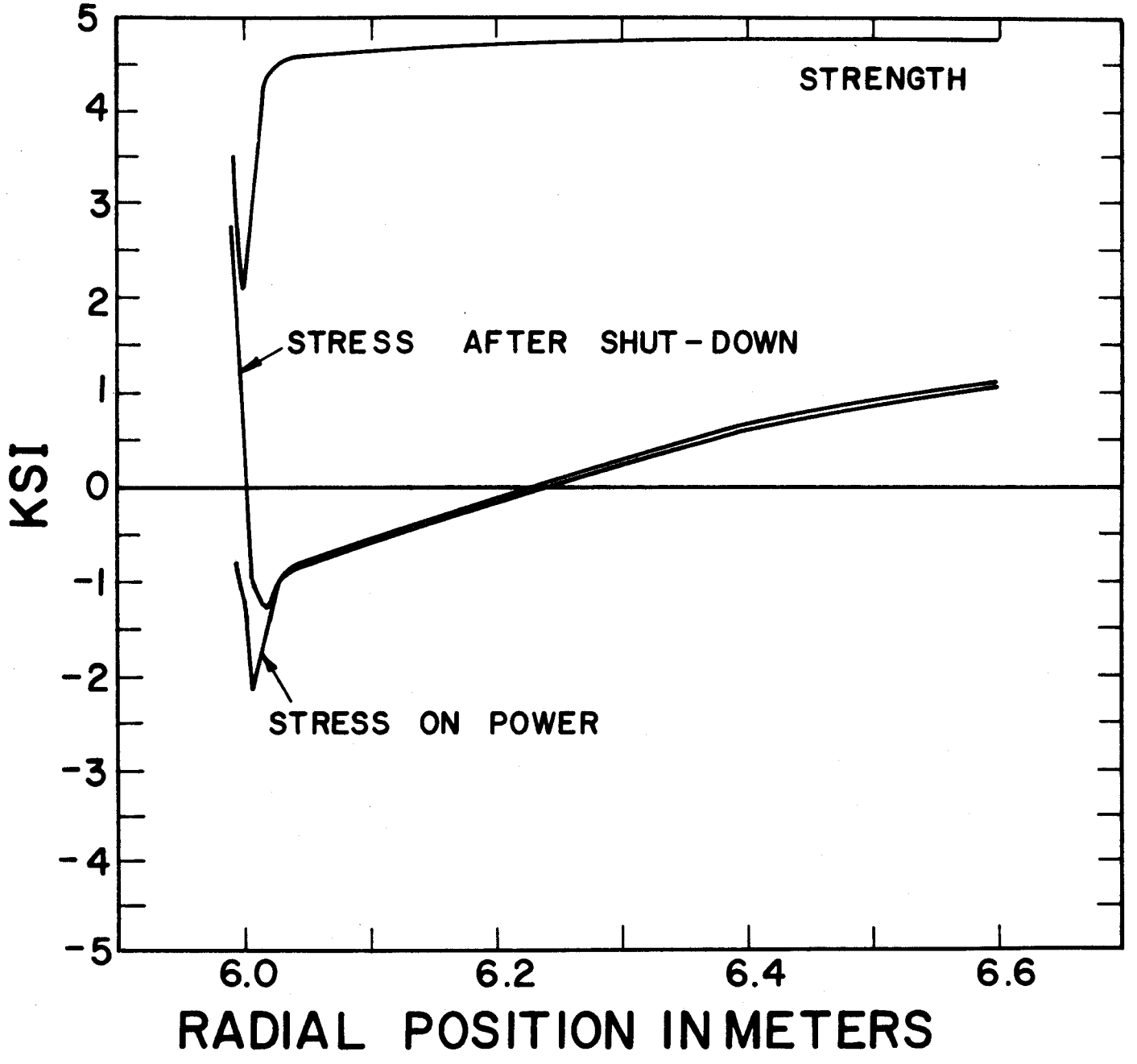

Fig. 34 Hoop Stress and Tensile Strength Distribution in the Radial Divider made of High-Growth Graphite with 5% Initial Porosity; After 0.4 Years of Irradiation.

The extent of the radial motion of an unrestrained divider can be seen from Fig. 35. Due to thermal expansion the outer boundary of the divider moves out about 2 cm during startup. In the course of the irradiation the graphite shrinks, and both boundaries start to reduce their radii. Since most of the graphite is never irradiated past the densification phase, the radial displacement of the boundaries is inward. After about one year the outer boundary radius is reduced by about 2 cm measured from the original radius of the cold structure. Therefore, the cold structure has a final radius of about 6.56 m on the outside and 5.94 on the inside.

III.4 Discussion of the Results

The major results of the inelastic analysis on a graphite structure in SOLASE can be summarized as follows:

1. The structure must not be rigidly restrained at its boundaries in order to avoid excessive thermal and swelling stresses.
2. Stresses generated internally by differential shrinkage and growth are sufficiently relieved during operation.
3. However, stresses on shutdown, mainly due to the reversal of thermal stresses, are life limiting.
4. The safe limit of the tensile strength reduces with increasing growth of the graphite porosity. This represents the other life-limiting factor.
5. Low-density graphite develops tensile stresses due to excessive shrinkage which when added to the reversed thermal stresses exceed the allowable tensile strength very early in life.

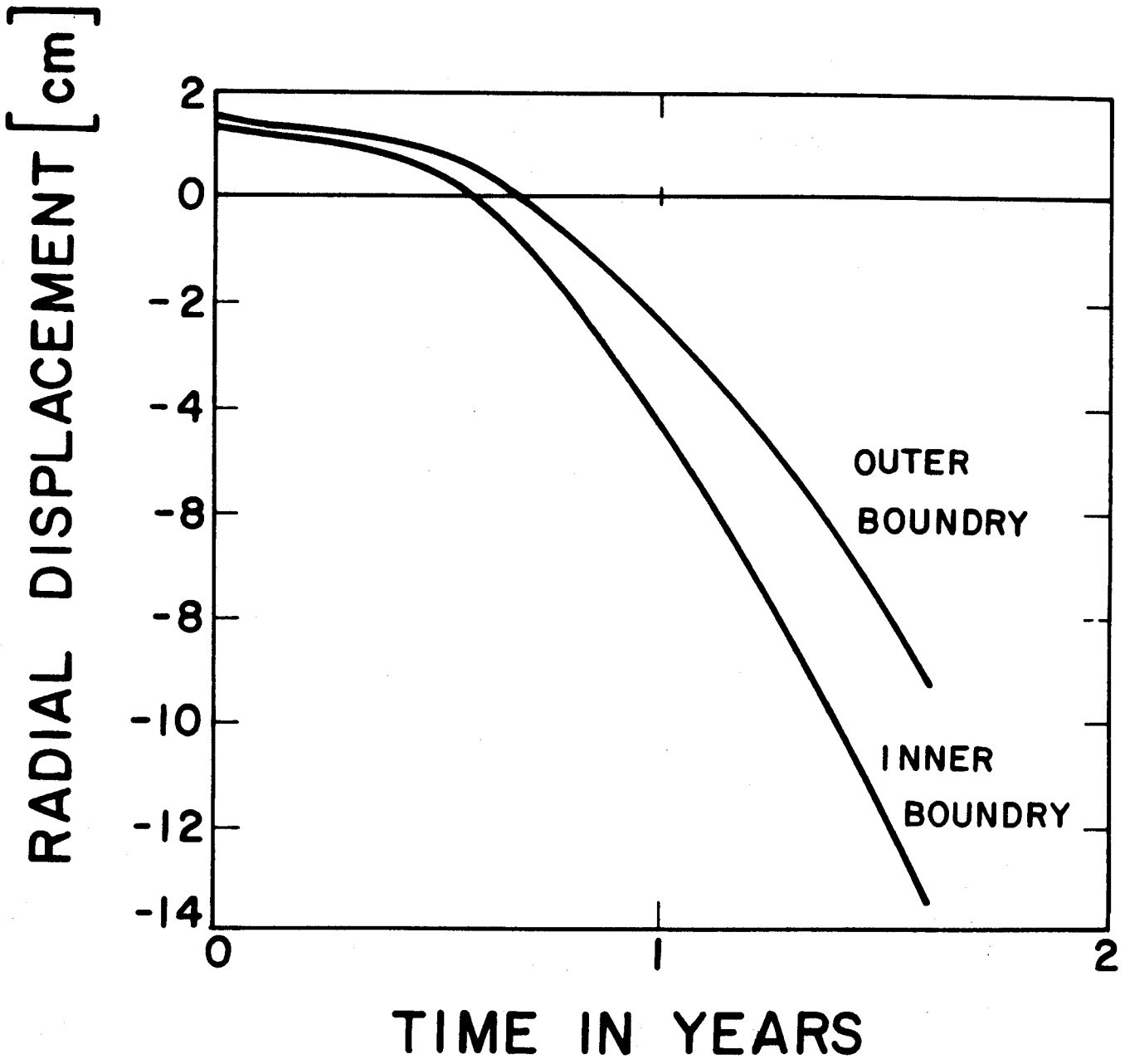

Fig. 35 The Radial Displacement of the Inner and Outer Boundaries of the Radial Divider made of Low-Growth Graphite with 5% Initial Porosity.

From these results we can draw a number of important conclusions.

The graphite structure must either be manufactured from a high-density-material (~ 5% initial porosity) or, possibly, a tailored density distribution must be designed so that the dense graphite is in the high-flux and medium-temperature region (~ 1000°C). The mechanical connections between the blanket structure and its surrounding support structure must be flexible. These two basic requirements are well within the range of present-day technology. Nevertheless, the behavior of graphite under irradiation was based on models which need further experimental verification, in particular with regard to irradiation at high temperatures (> 1200°C) and high fluences (> 10 dpa). Since the extrapolation of graphite behavior under irradiation was rather modest in this study, the results presented indicate that graphite is a suitable structural material for the blanket of fusion reactors, and lifetimes of about one year or more are realistic.

Within the scope of this study it was not possible to extend the analysis to the actual structure. Hence, the above conclusions are of a general nature.

It should be noted that more restrictive materials limitations often show up only after a more detailed structural analysis has been performed. Therefore, we recommend that future studies be directed towards a more comprehensive structural analysis and that they be performed in the same self-consistent fashion which was developed for this study. The inelastic analysis should, however, be generalized to anisotropic graphites. The need for such an analysis was perhaps best

demonstrated by the peculiar problem we encountered with low-density graphite. Problems of this kind can only be identified by detailed structural analysis.

References

1. W. N. Reynolds, "Physical Properties of Graphite", Elsevier Publ. Co. LTD., Amsterdam, 1968, Ch. VI.

2. B. T. Kelly, Nature 207, 257 (1965).

3. G. B. Engle, Carbon 9, 539 (1971).

4. W. C. Morgan, Nucl. Techn. 21, 50 (1974).

5. W. C. Morgan, E. M. Woodruff, and W. J. Gray in "Techn. of Controlled Nuclear Fusion",Vol. 1, CONF-760935-P1, p. 189 (1976).

6. W. J. Gray, W. C. Morgan in "Techn. of Controlled Thermonuclear Fusion Experiments and Eng. Aspects of Fusion Reactors", CONF-721111, p. 983.

7. M. Van den Berg, M. R. Everett, and A. Kingsbury, Proc. of the 12th Biennial Conf. on Carbon, Pittsburgh, 1975, p. 307.

8. R. Blackstone, J. Nucl. Matls. 65, 72 (1977).

9. H. J. Veringa and R. Blackstone, Carbon 14, 279 (1976)

10. J. E. Broklehurst, "Fracture in Polycrystalline Graphite" in Chemistry and Physics of Carbon, Vol. 13, Ed. by P. L. Walker, P. Tower, and M. Dekker, New York, 1977, p. 145.

11. R. M. Christensen, J. Mech. Phys. Solids 17, 23 (1969).

12. A similar, but less concise derivation of this problem can be found in the book of T. H. Lin, "Theory of Inelastic Structures", Wiley and Sons, New York, 1968, Chapter 7.

13. A. D. Whapham and M. J. Makin, Phil. Mag. 7, 1441 (1962).

14. R.W. Conn, et al., "SOLASE, A Conceptual Laser Fusion Reactor Design, University of Wisconsin Fusion Program Report UWFDM-220, Univ. of Wis., (December, 1977).

APPENDIX------- Stress Analysis Program Listing

```
@RUN WATSON,11162,5114816969,$5.00
@FOR,IS
      DIMENSION R(14),T(14),D(14),A(14),B(14),C(14),G(14),H(14)
      DIMENSION Q(14),U(14),O(14),P(14),T3(14),T4(14),Z3(14)
      DIMENSION E(14),Z4(14),P1(14),Z5(14)
      DIMENSION SIGULT(14,14),SIGON(14,14),SIGOF(14,14),TIME(14)
      DIMENSION RADIUS(14,14)
      DIMENSION NLINE(2),MASK(4000),RNOT(14)
      NLINE(1)=1
      NLINE(2)=2
      JJ=0
      N=14
      READ, (R(I),I=1,N)
      READ, (T(I),I=1,N)
      READ, (D(I),I=1,N)
      READ, (O(I),I=1,N)
      READ, (P(I),I=1,N)
      READ, (P1(I),I=1,N)
      PRINT,R
      PRINT,T
      PRINT,D
      PRINT,O
      PRINT,P
      PRINT,P1
      N0=0.2
      F0=5.E-3
      M=1
      Y0=0.001
      M2=1
      M7=0.
      ENLX=4.E-6
      IF (M.EQ.1) GO TO 540
      Z=2*((1+N0)*R(1)**2+(1-N0)*R(N)**2)
      C(1)=-(1+N0)/Z
      C(2)=-(1-N0)*R(N)**2/Z
      R(N)=6.6
      GO TO 590
  540 Z=2*(R(N)**2-R(1)**2)
      C(1)=1/Z
      C(2)=-(R(N)**2)/Z
      Q(1)=0
      Q(N)=0
C     INITIAL THERMAL STRESSES
  590 R0=R(1)
      A0=0
      A2=0
      DO 710 I=1,N
      T0=T(I)
      A1=ENLX*T0
      A(I)=A2+(A1+A0)*(R(I)**2-R0**2)/2
      A2=A(I)
      A0=A1
      R0=R(I)
      B(I)=0
```

```
  710 CONTINUE
      PRINT,Z
      PRINT,A
      C0=C(1)*A(N)
      DO 780 I=1,N
      T0=T(I)
      Z=(C0*R(1)**2+A(I)/2)/R(I)**2
      Q(I)=C0-Z
      U(I)=C0+Z-FNLX*T0
  780 CONTINUE
      PRINT,Q
      PRINT,U
      U0=0
      R0=R(1)
      W=0
      DO 860 I=1,N
      W=W+(U(I)+U0)*(R(I)-R0)/2
      PRINT,W
      U0=U(I)
      R0=R(I)
  860 CONTINUE
      W2=W-R(N)*Q(N)
      W=W/(R(N)-R(1))
      IF (M.EQ.2) GO TO 940
      DO 920 I=1,N
      U(I)=U(I)-W
  920 CONTINUE
      GO TO 970
  940 DO 960 I=1,N
      U(I)=U(I)-W2/(R(N)-R(1))
  960 CONTINUE
  970 DO 990 I=1,N
      T4(I)=U(I)
  990 CONTINUE
      Y=0.
      L=1
      PRINT,T4
C     TIME LOOP
      S0=P1(1)/100.
      PRINT,JJ,L,Y0,Y,Q(L)
      CALL PLOTTS(T,D,Y,P1,N0,F0,U,T4,N,R,B,A,C0,M7,Z3,Z4,Z5,T3,E,I)
      M=L
      DO 995 J=1,N
      SIGULT(J,M)=Z3(J)
      SIGON(J,M)=Z4(J)
      SIGOF(J,M)=T3(J)
      TIME(M)=Y
      RADIUS(J,M)=R(J)*2.5
  995 CONTINUE
 1050 M7=1
 1060 DO 1090 I=1,N
      IF (M2.EQ.2) GO TO 1100
      R(I)=R(I)+E(I)
 1090 CONTINUE
```

```
1100 IF (M.EQ.2) GO TO 1140
     Q(1)=0
     Q(N)=0
     GO TO 1150
1140 R(N)=6.6
1150 R0=R(1)
     A0=0
     A2=0
     B0=0
     B2=0
     DO 1380 I=1,N
     T0=T(I)
     D0=D(I)
     R1=R(I)
     CALL SSDOT(T0,D0,Y,P1,V0,V1,S,S0,I)
1250 CALL CREEP(T0,D0,J)
1260 A1= 2*S/3+J*(Q(I)+U(I))/2.
     B1=(3*J*(Q(I)-U(I))/2)/(R1**2)
     A(I)=A2+(A1+A0)*(R1**2-R0**2)/4
     IF (I.GT.1) GO TO 1320
     B(1)=0
     GO TO 1330
1320 B(I)=B2+(B1+B0)*(R1**2-R0**2)/2
1330 A2=A(I)
     B2=B(I)
     A0=A1
     B0=B1
     R0=R(I)
1380 CONTINUE
     C0=C(1)*A(N)+C(2)*B(N)
     DO 1490 I=1,N
     T0=T(I)
     D0=D(I)
     CALL SSDOT(T0,D0,Y,P1,V0,V1,S,S0,I)
1440 CALL CREEP(T0,D0,J)
1450 E0=S/3+J*(U(I)-Q(I)/2)
     Z=(C0*R(1)**2+A(I)/2)/(R(I)**2)
     Q(I)=Q(I)+(C0-Z+B(I)/2)*Y0
     U(I)=U(I)+(C0+Z+B(I)/2-E0)*Y0
1490 CONTINUE
     U0=0
     R0=R(1)
     W=0
     DO 1570 I=1,N
     W=(U(I)+U0)*(R(I)-R0)/2+W
     U0=U(I)
     R0=R(I)
1570 CONTINUE
     Y=Y+Y0
     JJ=JJ+1
     W2=W-R(N)*Q(N)
     W=W/(R(N)-R(1))
     IF (M.EQ.2) GO TO 1660
     DO 1640 I=1,N
```

```
      U(I)=U(I)-W
1640  CONTINUE
      GO TO 1690
1660  DO 1680 I=1,N
      U(I)=U(I)-W2/(R(N)-R(1))
1680  CONTINUE
1690  IF (JJ.NE.12) GO TO 1700
      Y=0.01
1700  IF (JJ.NE.18) GO TO 1701
      Y=0.02
1701  IF (JJ.NE.35) GO TO 1702
      Y=0.1
1702  IF (JJ.NE.56) GO TO 1703
      Y=0.2
1703  IF (JJ.NE.77) GO TO 1704
      Y=0.4
1704  IF (JJ.NE.98) GO TO 1705
      Y=0.6
1705  IF (JJ.NE.119) GO TO 1706
      Y=0.8
1706  IF (JJ.NE.140) GO TO 1707
      Y=1.0
1707  IF (JJ.NE.161) GO TO 1708
      Y=1.2
1708  IF (JJ.NE.182) GO TO 1709
      Y=1.4
1709  IF (JJ.NE.203) GO TO 1710
      Y=1.6
1710  IF (JJ.NE.224) GO TO 1711
      Y=1.8
1711  IF (JJ.NE.245) GO TO 1712
      Y=2.0
1712  IF (Y.LT.O(L)) GO TO 1740
      L=L+1
      YO=P(L)
      JJ=JJ+1
      PRINT,JJ,L,YO,Y,O(L)
      PRINT,R
1730  CALL PLOTTS(T,D,Y,P1,NO,FO,U,T4,N,R,B,A,CO,M7,Z3,Z4,Z5,T3,E,I)
      M=L
      DO 1735 J=1,N
      SIGULT(J,M)=Z3(J)
      SIGON(J,M)=Z4(J)
      SIGOF(J,M)=T3(J)
      TIME(M)=Y
      RADIUS(J,M)=R(J)*2.5
1735  CONTINUE
1740  IF (Y.GT.1.6) GO TO 1840
1750  CALL DISPLA(N,NO,R,B,A,CO,M7,YO,E)
1760  J1=N-1
      DO 1820 I=1,J1
      J=J+1
      IF (R(J).GT.R(I)) GO TO 1830
      PRINT 1810,I
```

```
 1810 FORMAT      ('-','WHOOPS, YOUR NODE POINTS HAVE KINKED',I5)
 1820 CONTINUE
 1830 GO TO 1060
 1840 PRINT,Y
      PRINT,R
      PRINT,Z3
      PRINT,Z4
      PRINT,Z5
      DO 1850 I=1,N
 1850 RNOT(I)=RADIUS(I,1)
      PRINT,RNOT
      PRINT,TIME
      PRINT,SIGON
      ORIENT=GRID3D('X=ROWS','LOWER',RNOT,TIME)
      AXES=AXVALS(6.0,6.6,'AUTO','RADIUS (METERS)$$',0.,1.6,'AUTO',
     *'TIME (YEARS)$$',-3.5,5.    ,'AUTO','HOOP STRESS (KSI)$$')
      CALL SURGEN(SIGON,14,14,14,ORIENT,-30.,45., 5., 5.,'CROSS',
     *NLINE,0.    ,AXES,MASK,'HOOP STRESS ON POWER$/$INITIAL POROSITY =
     *5%$$')
      CALL SURGEN(SIGOF,14,14,14,ORIENT,-30.,45., 5., 5.,'CROSS',
     *NLINE,0.    ,AXES,MASK,'HOOP STRESS OFF POWER$/$INITIAL POROSITY =
     *5%$$')
      STOP
C*******************************************************************************
      SUBROUTINE SSDOT(T0,D0,Y,P1,V0,V1,S,S0,I)
      DIMENSION P1(14)
      V0=1/((800/T0)**2+(T0/1250)**12)
      V1=0.01*(2+((T0-700)/210)**2)
      X=D0*Y
      Z=P1(I)/V1+X**2
      S=2*V0*(1.5*X**2/Z-X**4/Z**2)-P1(I)*V1*EXP(-V1*X)
      S=S*D0/100
      S0=(V0*X**3/Z-P1(I)*(1-EXP(-V1*X)))/100
      RETURN
C*******************************************************************************
      SUBROUTINE CREEP(T0,D0,J)
      J=(1.77533+0.01852*T0)*1.E-8+(0.0403*T0-5.4433)*0.1*D0
      RETURN
C*******************************************************************************
      SUBROUTINE PLOTTS(T,D,Y,P1,N0,F0,U,T4,N,R,B,A,C0,M7,Z3,Z4,Z5,T3,E,
     1I)
      DIMENSION T(N),D(N),P1(N),U(N),T4(N),R(N),B(N),A(N)
      DIMENSION Z3(N),Z4(N),Z5(N),T3(N),E(N)
      Z8=0.001
      DO 2320 I=1,N
      T0=T(I)
      D0=D(I)
      CALL SSDOT(T0,D0,Y,P1,V0,V1,S,S0,I)
      S0=S0+P1(I)/100.
      CALL SMOD(N0,S0,G9)
      Z3(I)=F0*SQRT(G9)/Z8
      Z4(I)=(U(I)/Z8)*G9
      Z5(I)=(T4(I)/Z8)*G9
      T3(I)=Z4(I)-Z5(I)
```

```
 2320 CONTINUE
 2580 CALL DISPLA(N,N0,R,B,A,C0,M7,Y0,E)
      RETURN
C*******************************************************************************
      SUBROUTINE SMOD(N0,S0,G9)
      G9=(7-5*N0)*(7+5*N0)*(1-S0)*(S0**(7./3)-1)+126*S0*(1-S0**(2./3))**
     12
      G9=15*(1-N0)*(7+5*N0)*(S0**(7./3)-1)/G9
      G9=1/(1+G9*S0)
      RETURN
C*******************************************************************************
      SUBROUTINE DISPLA(N,N0,R,B,A,C0,M7,Y0,E)
      DIMENSION R(N),B(N),A(N),E(N)
      DO 2790 I=1,N
      E(I)=(1-N0)*R(I)*B(I)/2
      E(I)=E(I)+(1+N0)*A(I)/(2*R(I))
      E(I)=E(I)+(1+N0)*R(1)**2*C0/R(I)
      E(I)=E(I)+(1-N0)*C0*R(I)
      IF (M7.EQ.0) GO TO 2790
      E(I)=Y0*E(I)
 2790 CONTINUE
      RETURN
C*******************************************************************************
      END
@GSP
 PLOTTER PEN/LIQ/.5,SPEED/SLOW
@XQT
6 6.003 6.006 6.01 6.02 6.03 6.04 6.06 6.1 6.2 6.3 6.4 6.5 6.6
1500 1200 1050 886 688 625 607 602 600 600 600 600 600 600
32.5 32.28 32.1 31.75 31.0 30.25 29.5 28 25 17.5 12 6.5 3.93 1.35
0.002 0.004 0.01 0.02 0.1 0.2 0.4 0.6 0.8 1 1.2 1.4 1.6 1.8
.001 .001 .001 .002 .005 .005 .01 .01 .01 .01 .01 .01 .01 .01
5 5 5 5 5 5 5 5 5 5 5 5 5 5
```